

Bayesian multi-model estimation for fault slip distribution: the effect of prior constraints in the estimation for slow slip events beneath the Bungo Channel, southwest Japan

Ryoichiro Agata¹, Ryoko Nakata², Amato Kasahara³, Yuji Yagi⁴, Yukinari Seshimo⁵, Shoichi Yoshioka⁵, and Takeshi Iinuma¹

¹Japan Agency for Marine-Earth Science and Technology

²Tohoku University

³Independent researcher

⁴University of Tsukuba

⁵Kobe University

November 24, 2022

Abstract

We consider a Bayesian multi-model fault slip estimation (BMMFSE), in which many candidates of the underground-structure model characterized by a prior probability density function (PDF) are retained for a fully Bayesian estimation of fault slip distribution to manage model uncertainty properly. We performed geodetic data inversions to estimate slip distribution in long-term slow slip events (L-SSEs) that occurred beneath the Bungo Channel, southwest Japan, in around 2010 and 2018, focusing on the two advantages of BMMFSE: First, it allows for estimating slip distribution without introducing strong prior information such as smoothing constraints, handling an ill-posed inverse problem by combining a full Bayesian inference and accurate consideration of model uncertainty to avoid overfitting; second, the posterior PDF for the underground structure is also obtained through a fault slip estimation, which enables the estimation of sequential events by reducing the model uncertainty. The estimated slip distribution obtained using BMMFSE agreed better with the distribution of deep tectonic tremors at the down-dip side of the main rupture area than those obtained based on strong prior constraints in terms of the spatial distribution of the Coulomb failure stress change. This finding suggests a mechanical relationship between the L-SSE and the synchronized tremors. The use of the posterior PDF for the underground structure updated by the estimation for the 2010 L-SSE as an input of the analysis for the one in 2018 resulted in a more preferable Bayesian inference, indicated by a smaller value of an information criterion.

Abstract

We consider a Bayesian multi-model fault slip estimation (BMMFSE), in which many candidates of the underground-structure model characterized by a prior probability density function (PDF) are retained for a fully Bayesian estimation of fault slip distribution to manage model uncertainty properly. We performed geodetic data inversions to estimate slip distribution in long-term slow slip events (L-SSEs) that occurred beneath the Bungo Channel, southwest Japan, in around 2010 and 2018, focusing on the two advantages of BMMFSE: First, it allows for estimating slip distribution without introducing strong prior information such as smoothing constraints, handling an ill-posed inverse problem by combining a full Bayesian inference and accurate consideration of model uncertainty to avoid overfitting; second, the posterior PDF for the underground structure is also obtained through a fault slip estimation, which enables the estimation of sequential events by reducing the model uncertainty. The estimated slip distribution obtained using BMMFSE agreed better with the distribution of deep tectonic tremors at the down-dip side of the main rupture area than those obtained based on strong prior constraints in terms of the spatial distribution of the Coulomb failure stress change. This finding suggests a mechanical relationship between the L-SSE and the synchronized tremors. The use of the posterior PDF for the underground structure updated by the estimation for the 2010 L-SSE as an input of the analysis for the one in 2018 resulted in a more preferable Bayesian inference, indicated by a smaller value of an information criterion.

Plain Language Summary

This study attempts to accurately estimate moves between two plates for the occurrence of slow slip events (SSEs), which are slow earthquakes that do not produce seismic waves, targeting those occurred in southwest Japan. This was accomplished by analyzing satellite data of ground movement during the SSEs using a novel approach called the Bayesian multi-model fault slip estimation (BMMFSE) framework, which considers multiple candidates of assumptions for Earth structures. BMMFSE stabilizes the analysis and removes artifacts from the estimation results which are otherwise introduced because of the choice of a wrong Earth model. These advantages were validated by comparing the estimation results obtained based on previous approaches that do not consider multiple Earth models. The result of BMMFSE exhibited spatial distributions of fault moves that are more consistent with other slow earthquakes which occurred synchronously in the nearby fault. The method also sequentially revised the multiple Earth models and produced a better ensemble of the candidate models through the analyses of repeating SSEs.

1 Introduction

Accurately estimating slip distribution using seismic waveforms and geodetic data is essential to better understand earthquake rupture and preparation processes underground, such as interplate coupling. Recent advances in seismological and geodetic observation techniques have led to the recognition of a new class of fault slip that is transitional between the fast rupture and stable sliding on the plate interface, which are known as slow earthquakes. Slow slip event (SSE) is a type of slow earthquake whose characteristic time scale is days (short-term SSE or S-SSE) to years (long-term SSE or L-SSE). The response signal of an SSE is usually detectable by geodetic measurements (Obara & Kato, 2016), from which the slip distribution can be inferred. The occurrence of both L-SSEs and S-SSEs is often accompanied by an increase in the number of smaller events, in terms of both the amount of seismic moment release and the time scale, in the surrounding area.

74 For example, there have been many observations of S-SSEs associated with deep
 75 tectonic tremors, known as episodic tremor and slips (ETS) (e.g., Cascadia subduc-
 76 tion zone (Rogers & Dragert, 2003), Nankai trough subduction zone (Obara et al.,
 77 2004), etc.). Some L-SSEs are known to induce an increase in the number of sur-
 78 rounding tremors (e.g., the Bungo Channel in southwest Japan (Hirose et al., 2010),
 79 the Guerrero subduction zone (Kostoglodov et al., 2010; Villafuerte & Cruz-Atienza,
 80 2017), etc.), and swarm-like seismic activities (for example, the Boso Peninsula in
 81 central Japan (Hirose et al., 2014), and the Hikurangi subduction zone (Bartlow et
 82 al., 2014). To investigate the generation process of slow earthquakes, spatial rela-
 83 tionships between the estimated slip distribution for SSEs and hypocenter locations
 84 of such small events have been particularly studied (the readers are referred to the
 85 aforementioned articles). In addition, slip distribution occurring in SSEs that oc-
 86 cur repeatedly in the same region has been analyzed simultaneously (Bartlow et
 87 al. (2014); Yoshioka et al. (2015); Takagi et al. (2019); Hirose and Kimura (2020)
 88 and many others), in part because the interval between each event is relatively short
 89 compared to ordinary earthquakes of the same level of seismic moment release. Com-
 90 parisons of slip distributions in such repeating events may be useful for detecting
 91 temporal changes in the interseismic coupling rate or stress conditions in the sur-
 92 rounding seismogenic zones.

93 **1.1 Faults slip estimation and uncertainty of the underground struc-** 94 **ture**

95 Regardless of targeting ordinary earthquakes or SSEs, the estimation of fault
 96 slip distribution is usually performed in a two-step procedure (e.g., pointed out by
 97 Fukahata and Matsu'ura (2006)): The first step is to set a numerical model that
 98 describes the characteristics of the media in the target domain of the Earth. A nu-
 99 merical model of the underground structure (which in principle consists of an elas-
 100 tic structure and the geometry of the fault plane in this study) is assumed by re-
 101 ferring to databases proposed by previous studies based on many observations. In
 102 parametrizing the slip distribution in the assumed underground structure model, the
 103 slip parameters and the response at the observation points are usually described by
 104 a linear relationship (in many cases, based on linear elasticity). In the second step,
 105 the parameters that describe the slip distribution are estimated using observation
 106 data based on a linear relationship. This approach assumes that the earth model is
 107 associated with no uncertainty because a single underground structure model is cho-
 108 sen in the first step and other possibilities for model selection are discarded. This
 109 assumption allows for simplification by formulating the slip estimation as a simple
 110 linear inverse problem, which has been widely applied in previous studies. However,
 111 such an assumption often underestimates the amount of error in the prediction made
 112 by the model, which can lead to overfitting in estimation and obtaining a biased es-
 113 timation result (e.g., Yagi and Fukahata (2008, 2011)).

114 To avoid such overfitting and bias in estimations, some approaches for con-
 115 sidering model uncertainty in fault slip estimation have been proposed. The most
 116 straightforward approach is to estimate the parameters of the slip distribution and
 117 those that characterize the underground structure simultaneously (e.g., Fukahata
 118 and Wright (2008); Fukuda and Johnson (2010); Minson et al. (2014); Agata et al.
 119 (2018); Shimizu et al. (2021)). Another approach is to introduce the contribution
 120 of the model prediction errors to the covariance components in the data covariance
 121 matrix. Yagi and Fukahata (2011) proposed an inversion scheme that introduces
 122 the error of Green's functions following a Gaussian distribution and iteratively es-
 123 timates the model parameters and the covariance matrix for the model prediction
 124 errors simultaneously. Duputel et al. (2014) proposed a comprehensive framework
 125 to compute the covariance matrix that considers the stochastic property of model
 126 prediction errors based on uncertain and presumably inaccurate prior knowledge of

127 the underground elastic structure. These methods are known to relax the effect of
 128 overfitting in the estimation of fault slip distribution owing to the choice of a single
 129 underground structure model. However, the former approach based on simultaneous
 130 estimation usually adds unknowns that are in a nonlinear relationship with the re-
 131 sponse in observation stations to the target estimation problem. In such a case, it is
 132 necessary to perform the forward simulation iteratively to obtain a converged solu-
 133 tion. The calculation cost associated with iterative analysis may limit the range of
 134 applicable problems. The latter approach, which introduces the covariance compo-
 135 nents, retains a linear relationship between unknown parameters and the observation
 136 response, which avoids iterative executions of the forward simulation within the esti-
 137 mation scheme. However, this approach procures no information on the underground
 138 structure that is intrinsically included in the data. In addition, it is based on the as-
 139 sumption that the model prediction errors follow a Gaussian distribution, which may
 140 be violated when the model uncertainty is large.

141 Recently, Agata et al. (2021) proposed a flexible framework of Bayesian infer-
 142 ence for slip estimation considering model uncertainty, which introduces many candi-
 143 dates for underground structure models, whose characteristic parameters follow a
 144 prior probability density function (PDF), instead of choosing a single model in the
 145 “first step” of the process of a usual fault slip inversion. This approach allows for
 146 the estimation of slip parameters considering a wider range of underground struc-
 147 ture parameters while avoiding non-linear parameters to be included in the estima-
 148 tion. Such treatment is enabled by eliminating the underground structure param-
 149 eters by marginalization in advance of Bayesian sampling for the posterior PDF of
 150 the slip parameters. Furthermore, the posterior PDF for the underground structure
 151 can be obtained in a post process of Bayesian sampling. In addition, the formula-
 152 tion of the work corresponds to the generalization of the one proposed in Duputel et
 153 al. (2014) in that the framework of Agata et al. (2021) is not limited to applications
 154 assuming the Gaussian distribution but allows for an arbitrary probability distri-
 155 bution by using an ensemble approximation. We can also interpret the framework
 156 in the context of Bayesian multi-model estimation, originally called Bayesian model
 157 averaging (Raftery et al., 1997), in which multiple candidate models are simulta-
 158 neously considered and the contribution from each model in explaining the data is
 159 scored following Bayes’ theorem, aiming to increase the generalization ability of the
 160 Bayesian model. Therefore, we hereafter refer to the approach of Agata et al. (2021)
 161 as Bayesian multi-model fault slip estimation (BMMFSE). Thus, the BMMFSE is a
 162 generalized framework that considers the uncertainty of the underground structure
 163 in fault slip estimation. Although the advantages of using BMMFSE in fault slip in-
 164 version are discussed in detail in Agata et al. (2021), the method was only applied to
 165 a very simple numerical experiment. In the present study, we apply the method to
 166 estimate the slip distribution in SSEs, focusing on two advantages of BMMFSE.

167 **1.2 Advantages of using BMMFSE for analyses of SSEs**

168 One advantage is that BMMFSE allows for easier handling of the ill-posedness
 169 of slip estimation by introducing a fully Bayesian inference. In general, slip esti-
 170 mation is an ill-posed inverse problem, which is usually handled based on regular-
 171 ization by incorporating prior information on the characteristics of the slip distri-
 172 bution, such as smoothness and sparseness. The introduction of such information,
 173 which we hereafter call “strong prior” to distinguish it from weakly informative pri-
 174 ors mentioned later, allows for obtaining a unique and stable solution by minimiz-
 175 ing an objective function. Fully Bayesian inference is another approach to handle
 176 ill-posedness, which was recently introduced to fault slip estimation (e.g., Fukuda
 177 and Johnson (2008, 2010)): An ensemble of the solutions sampled from the poste-
 178 rior PDF is obtained in combination with weakly informative prior information for
 179 slip distribution, such as uniform distribution for the slip amount in each fault patch

(e.g., Minson et al. (2013)). However, slip estimation using such weakly informative prior PDFs for slip distribution is prone to suffer more severely from overfitting to data errors. To avoid overfitting, accurately considering the model prediction errors originating from the uncertainty of the underground structure, which is often a major component of data errors (Duputel et al., 2014), by introducing BMMFSE is expected to be effective. Performing slip estimation based only on weakly informative prior PDFs has the potential to enable a more careful investigation of the spatial relationships between the estimated slip distribution of SSEs and hypocenter locations of the surrounding events: An investigation on the correspondence between the estimated slip distribution in SSEs and synchronized tremor hypocenters in the Cascadia subduction zone suggest that incorporation of strong prior constraints for slip distribution, such as spatial and temporal smoothing constraints, significantly affects the conclusion (Bartlow et al., 2011). In addition, a fused lasso method (Tibshirani et al., 2005), which promotes both sparsity and smoothness of the parameter distribution using L1-norm-based penalization, has also been applied to L-SSEs occurring beneath the Bungo Channel and found to be more effective for detecting discontinuous boundaries of the fault slip than using a widely used smoothing constraint based on a finite-difference approximation of the Laplacian operator (Nakata et al., 2017). This finding reconfirms the effect of the choice of regularization scheme on the estimation results of slip distribution.

The other advantage is that BMMFSE obtains the posterior PDF of the underground structure parameters in addition to those for the slip distribution. This means that the posterior PDF for the underground structure obtained in the analysis can be plugged into another estimation as the prior PDF. Such a method may be useful for further reducing the model prediction errors and validating the posterior PDF of the underground structure model obtained for each event. The estimation of SSEs occurring repeatedly at the same location can be a good application example of such a sequential estimation updating the underground structure.

1.3 Objectives

In this study, we estimate the posterior PDFs of the slip distribution of L-SSEs using BMMFSE, taking into account the uncertainty of the underground structure model by introducing many candidate models. We target L-SSEs that occurred beneath the Bungo Channel, southwest Japan, because of three features of these events: an increase in the number of deep tectonic tremors accompanying the L-SSEs was observed at the down-dip side of the main rupture area; multiple types of strong prior constraints have been applied to estimate past events; they occur repeatedly every six to eight years in almost the same location. These are the typical features of SSE for which BMMFSE may be advantageous, as explained in the last paragraph. For this purpose, we constructed a multi (ensemble) model to describe the uncertainty of the underground structure around the rupture area based on the database of the elastic structure and geometry of the plate boundary defined for southwest Japan and introduced it to the fully Bayesian inference of slip distribution. Thus, we estimated the posterior PDF for the slip distribution in the L-SSE that occurred around 2010 and 2018 using weakly informative prior PDFs. We compared the up- and down-dip limits of the slip distribution estimated based on BMMFSE and strong prior constraints in examining the spatial relationship with synchronized slow earthquakes in the surrounding regions. We also demonstrate a sequential estimation of the L-SSEs updating the underground structure by estimating the slip distribution in the 2018 L-SSE based on multiple models that describe the posterior PDF of the underground structure obtained in the estimation for the 2010 L-SSE. We examine the validity of the approach using an information criterion.

2 Observation data

The occurrence of L-SSEs beneath the Bungo Channel in southwest Japan, well known because of the continuous observation by the Global Navigation Satellite System (GNSS) conducted by the GNSS Earth Observation Network System (GEONET) (Miyazaki & Hatanaka, 1998) and managed by the Geospatial Information Authority of Japan, was observed repeatedly around 1997, 2003, 2010, and 2018. The main rupture areas of these four events are estimated to nearly coincide (Yoshioka et al., 2015; Ozawa et al., 2020; Seshimo & Yoshioka, 2021), filling a spatial gap between the deep ETS and seismogenic zones (Figure 1). Activities of deep tectonic tremors at the down-dip side and shallow very-low-frequency earthquakes (VLFEs) in the south of the main rupture area have shown rapid increases simultaneously with the acceleration phase of the L-SSEs (Hirose et al., 2010). Recent developments in data analysis techniques for GNSS data suggest that these major L-SSEs are accompanied by minor events of a smaller seismic moment release, which occurs nearly in the middle of the periods between the major events (Takagi et al., 2019). In this study, we focus on two recent major L-SSEs in this region that occurred around 2010 and 2018.

We used digital data for the observed vertical and horizontal displacements of the 2010 and 2018 L-SSEs (Figure 2), the former of which were provided by Yoshioka et al. (2015). The data for the latter were newly processed by Seshimo and Yoshioka (2021) based on the same approach of data analysis as that used in Yoshioka et al. (2015). The data were processed from the crustal displacements observed by GEONET. In all, we used 106 and 96 continuous GNSS stations in the estimation for the 2010 and 2018 events, respectively (some stations are excluded from the estimation for the latter event to avoid contaminating the displacement data with post-seismic deformation due to the 2016 Kumamoto earthquake following Seshimo and Yoshioka (2021)). We used only the total displacement of each component during periods from 2009.5 to 2011.2 and 2018.9 to 2019.5 in the decimal form, respectively. The dataset used for the 2010 L-SSE is identical to that used for the analyses of the same event in Nakata et al. (2017). We focused only on the spatial distribution to estimate the detailed distribution of the total slips during each L-SSE.

3 Estimation of the posterior PDF for the slip distribution considering the uncertainty of the underground structure

3.1 Formulation

We provide a summary of the formulation of BMMFSE, a method to estimate the posterior PDF for the slip distribution considering the uncertainty of the underground structure proposed by Agata et al. (2021). Let us consider an estimation problem of \mathbf{m} , which is a vector for the parameters of the slip distribution, from \mathbf{d} , a vector for the observation data. A widely used Bayesian formulation for estimating the posterior PDF for slip distribution, where a single underground structure model is chosen a priori, is written as follows:

$$P(\mathbf{m}|\mathbf{d}) = \kappa P(\mathbf{d}|\mathbf{m})P(\mathbf{m}), \quad (1)$$

where $P(\mathbf{m}|\mathbf{d})$, $P(\mathbf{d}|\mathbf{m})$, and $P(\mathbf{m})$ are the posterior PDF of the slip parameters, the likelihood function, and the prior PDF of the slip parameters, respectively. $\kappa = 1/P(\mathbf{d})$ is a normalization factor that takes a constant value because the observation data and model are fixed. However, it is natural to assume that the probabilistic density for the model prediction described by $P(\mathbf{d}|\mathbf{m})$ also depends on the choice of the underground structure model, which we hereafter characterize using parameters $\boldsymbol{\varphi}$. This dependence can be incorporated in the likelihood function as $P(\mathbf{d}|\mathbf{m}, \boldsymbol{\varphi})$. Let us suppose that we know the PDF $P(\boldsymbol{\varphi})$ to describe the stochastic property of

280 the uncertainty of the underground structure. Then, a posterior PDF for \mathbf{m} con-
 281 sidering the uncertainty of $\boldsymbol{\varphi}$ can be obtained by replacing the original likelihood
 282 function with $P(\mathbf{d}|\mathbf{m}, \boldsymbol{\varphi})$ and marginalizing the right-hand side with $\boldsymbol{\varphi}$, as

$$P(\mathbf{m}|\mathbf{d}) = \int P(\mathbf{m}, \boldsymbol{\varphi}|\mathbf{d})d\boldsymbol{\varphi}, \quad (2)$$

$$= \kappa \int P(\mathbf{d}|\mathbf{m}, \boldsymbol{\varphi})P(\mathbf{m}|\boldsymbol{\varphi})P(\boldsymbol{\varphi})d\boldsymbol{\varphi}. \quad (3)$$

283 The widely used approach described by Equation 1 corresponds to a case in which
 284 $\boldsymbol{\varphi}$ is fixed a priori in Equation 3, that is, $P(\boldsymbol{\varphi}) = \delta(\boldsymbol{\varphi} - \boldsymbol{\varphi}_{\text{fix}})$, that is, a single
 285 model is chosen in the “first step” described in Section 1. Here, we consider a sit-
 286 uation in which uncertain information of the underground structure is available in
 287 the form of an ensemble consisting of random samples $\boldsymbol{\varphi}^{(n)}$ drawn from $P(\boldsymbol{\varphi})$, where
 288 $n = 1, \dots, N$, and N are sufficiently large numbers. By using the samples, the inte-
 289 gration on the right-hand side of Equation 3 can be approximately evaluated based
 290 on Monte Carlo integration as:

$$P(\mathbf{m}|\mathbf{d}) = \kappa \int P(\mathbf{d}|\mathbf{m}, \boldsymbol{\varphi})P(\mathbf{m}|\boldsymbol{\varphi})P(\boldsymbol{\varphi})d\boldsymbol{\varphi} \quad (4)$$

$$\simeq \kappa \frac{1}{N} \sum_{n=1}^N P(\mathbf{d}|\mathbf{m}, \boldsymbol{\varphi}^{(n)})P(\mathbf{m}|\boldsymbol{\varphi}^{(n)}). \quad (5)$$

291 Providing the likelihood function \mathbf{d} , $P(\mathbf{d}|\mathbf{m}, \boldsymbol{\varphi})$ in the form of a parametric distri-
 292 bution allows for the explicit calculation of the density $P(\mathbf{m}|\mathbf{d})$ for a given \mathbf{m} . In
 293 this study, we assumed a simple Gaussian distribution for the likelihood function as
 294 follows:

$$P(\mathbf{d}|\mathbf{m}, \boldsymbol{\varphi}) = (2\pi)^{-N_d/2} |\mathbf{E}|^{-1/2} \exp[-\frac{1}{2}(\mathbf{d} - \mathbf{G}(\boldsymbol{\varphi})\mathbf{m})^T \mathbf{E}^{-1}(\mathbf{d} - \mathbf{G}(\boldsymbol{\varphi})\mathbf{m})], \quad (6)$$

295 where N_d , \mathbf{E} , and $\mathbf{G}(\boldsymbol{\varphi})$ are the dimensions of the data vector, the covariance ma-
 296 trix that is determined based on the error characteristics of the observation instru-
 297 ments and data processing, and the response matrix that relates the slip parameters
 298 and the response in the observation stations calculated based on elasticity for the
 299 given $\boldsymbol{\varphi}$, respectively. Thus, we can draw random samples of \mathbf{m} from the posterior
 300 PDF $P(\mathbf{m}|\mathbf{d})$ using sampling methods such as Markov chain Monte Carlo (MCMC)
 301 methods (e.g., Metropolis et al. (1953)). We use the replica-exchange Monte Carlo
 302 method (REMC; Swendsen and Wang (1986); Geyer (1991)), which is also known as
 303 parallel tempering, an acceleration method of MCMC sampling.

304 The formulation of BMMFSE presented so far is based on Bayes’ theorem for
 305 the joint posterior PDF for \mathbf{m} and $\boldsymbol{\varphi}$. Interestingly, the same formulation can be
 306 obtained from a different starting point, that is, considering the variability in the
 307 model prediction defined by the likelihood function in the conventional formulation
 308 presented in Equation 1, as

$$P(\mathbf{d}|\mathbf{m}) = \int P(\mathbf{d}|\mathbf{d}_{\text{pred}})P(\mathbf{d}_{\text{pred}}|\mathbf{m})d\mathbf{d}_{\text{pred}}, \quad (7)$$

309 where \mathbf{d}_{pred} and $P(\mathbf{d}_{\text{pred}}|\mathbf{m})$ denote the predicted response at the observation point
 310 and the stochastic property of the model prediction for a given \mathbf{m} , respectively. This
 311 marginalization (integration) for \mathbf{d}_{pred} can be approximately conducted by Monte
 312 Carlo integration, resulting in the same calculation as presented in Equation 5 (see
 313 Section 2 of Agata et al. (2021) for details). This alternative derivation essentially
 314 suggests that the BMMFSE corresponds to a generalization of the formulation of
 315 Duputel et al. (2014) to a non-Gaussian scheme.

316 Once we obtain the samples of \mathbf{m} and the values of the likelihood function as-
 317 sociated with the samples via MCMC sampling, we can also approximate the poste-
 318 rior PDF of $\boldsymbol{\varphi}$. By replacing the marginalization in Equation 2 with one based on \mathbf{m}

319 with further transformation, we obtain

$$P(\boldsymbol{\varphi}|\mathbf{d}) = \int P(\mathbf{m}, \boldsymbol{\varphi}|\mathbf{d})d\mathbf{m}, \quad (8)$$

$$= \int P(\boldsymbol{\varphi}|\mathbf{m}, \mathbf{d})P(\mathbf{m}|\mathbf{d})d\mathbf{m} \quad (9)$$

$$= \int \frac{P(\mathbf{d}|\mathbf{m}, \boldsymbol{\varphi})P(\boldsymbol{\varphi}|\mathbf{m})}{\int P(\mathbf{d}|\mathbf{m}, \boldsymbol{\varphi}')P(\boldsymbol{\varphi}'|\mathbf{m})d\boldsymbol{\varphi}'}P(\mathbf{m}|\mathbf{d})d\mathbf{m}, \quad (10)$$

320 where we use the relation $P(\boldsymbol{\varphi}|\mathbf{m}, \mathbf{d}) = P(\mathbf{d}|\mathbf{m}, \boldsymbol{\varphi})P(\boldsymbol{\varphi}|\mathbf{m})/P(\mathbf{d}|\mathbf{m})$ and $P(\mathbf{d}|\mathbf{m}) =$
 321 $\int P(\mathbf{d}|\mathbf{m}, \boldsymbol{\varphi}')P(\boldsymbol{\varphi}'|\mathbf{m})d\boldsymbol{\varphi}'$ in the transformation of Equation 9 to 10. Suppose we
 322 have obtained M samples from $P(\mathbf{m}|\mathbf{d})$ based on the REMC sampling, because we
 323 set $P(\boldsymbol{\varphi}|\mathbf{m}) = P(\boldsymbol{\varphi})$ in the present problem, we can rewrite the equation and ap-
 324 proximate $P(\boldsymbol{\varphi}|\mathbf{d})$ based on the Monte Carlo integration as

$$P(\boldsymbol{\varphi}|\mathbf{d}) = \int \frac{P(\mathbf{d}|\mathbf{m}, \boldsymbol{\varphi})P(\boldsymbol{\varphi})}{\int P(\mathbf{d}|\mathbf{m}, \boldsymbol{\varphi}')P(\boldsymbol{\varphi}')d\boldsymbol{\varphi}'}P(\mathbf{m}|\mathbf{d})d\mathbf{m} \quad (11)$$

$$\simeq \frac{1}{M} \sum_{m=1}^M \frac{P(\mathbf{d}|\mathbf{m}^{(m)}, \boldsymbol{\varphi})P(\boldsymbol{\varphi})}{\frac{1}{N} \sum_{n=1}^N P(\mathbf{d}|\mathbf{m}^{(m)}, \boldsymbol{\varphi}^{(n)})}. \quad (12)$$

325 $P(\boldsymbol{\varphi})$ can be approximated using the same N samples of $\boldsymbol{\varphi}$ as those used for the
 326 Monte Carlo integration in Equation 5 and others by, for example, an approximation
 327 based on the Monte Carlo method as follows:

$$\hat{P}(\boldsymbol{\varphi}) = \frac{1}{N} \sum_{n=1}^N \delta(\boldsymbol{\varphi} - \boldsymbol{\varphi}^{(n)}), \quad (13)$$

328 where $\delta(\boldsymbol{\varphi} - \boldsymbol{\varphi}^{(n)})$ is a delta function that satisfies

$$\delta(\mathbf{x}) = \mathbf{0} \quad (\mathbf{x} \neq \mathbf{0}), \quad (14)$$

329 and

$$\int_{\mathbf{S}} f(\mathbf{x})\delta(\mathbf{x} - \mathbf{x}^*)d\mathbf{x} = \begin{cases} f(\mathbf{x}^*) & (\mathbf{x}^* \in \mathbf{S}) \\ 0 & (\mathbf{x}^* \notin \mathbf{S}). \end{cases} \quad (15)$$

330 By substituting this term into $P(\boldsymbol{\varphi})$ in Equation 12, the marginal posterior PDF of
 331 $\boldsymbol{\varphi}$ can also be written based on the approximation by the Monte Carlo method as

$$\hat{P}(\boldsymbol{\varphi}|\mathbf{d}) = \frac{1}{N} \sum_{n=1}^N w^{(n)}\delta(\boldsymbol{\varphi} - \boldsymbol{\varphi}^{(n)}), \quad (16)$$

332 where

$$w^{(n)} = \frac{1}{M} \sum_{m=1}^M \frac{P(\mathbf{d}|\mathbf{m}^{(m)}, \boldsymbol{\varphi}^{(n)})}{\frac{1}{N} \sum_{n'=1}^N P(\mathbf{d}|\mathbf{m}^{(m)}, \boldsymbol{\varphi}^{(n')})}. \quad (17)$$

333 Because $P(\mathbf{d}|\mathbf{m}^{(m)}, \boldsymbol{\varphi}^{(n)})$ is already calculated when REMC sampling for $P(\mathbf{m}|\mathbf{d})$ is
 334 performed, as shown in Equation 5, we can readily evaluate $w^{(n)}$.

335 The formulation presented here and used in the following applications is based
 336 on the simplest approximation of $P(\boldsymbol{\varphi})$ using the delta function without weights.
 337 Other forms of the approximation of $P(\boldsymbol{\varphi})$ are also applicable to the proposed ap-
 338 proach. For example, importance weighting can be used to enhance the approxima-
 339 tion based on the delta function (see Appendix A for details).

340
341

3.2 Multiple models to describe the uncertainty property of plate boundary geometry and elastic structure model

342
343
344
345
346
347
348
349
350
351
352

We consider the static linear elasticity to relate the fault slip underground to displacement on the surface based on a two-layered underground structure model consisting of a half-space and a layer above it, corresponding to the mantle and crust, respectively. The slips are located on a curved surface that models the plate boundary. We assume that φ consists of parameters for the plate boundary geometry and elastic parameters, namely, rigidity and Poisson's ratio, which are calculated from the seismic velocity and density structure. Provided that the underground structure model possesses a certain amount of uncertainty, we consider an ensemble of multiple models to describe the uncertain property by setting properly $P(\varphi)$ based on the published models, to avoid bias in the estimation because of an a priori selection of φ_{fix} and overfitting.

353
354
355
356
357
358
359
360
361
362
363
364
365
366

Several geometry models for the plate boundary, including the Nankai Trough region, have been published. Here, we consider three models: Iwasaki et al. (2015), Hayes et al. (2018), and Nakanishi et al. (2018), which are hereafter referred to as the Iwasaki, Slab2, and Nakanishi models, respectively (Figure 3). The Iwasaki model is mainly based on the hypocenter distribution for the geometry with longer wavelengths, refined by results from seismic tomography, receiver function analysis, and active source experiment. Slab2 focuses more on comprehensive modeling on a global scale. The Nakanishi model is based on more detailed seismic survey results in the shallower part, while the deeper part is based on seismicity. We consider an ensemble of multiple models for the plate boundary geometry, assuming that the true plate boundary geometry can be modelled sufficiently well by one of the models based on a weighted average of the depth of the three geometry models, that is, the plate boundary geometry in the n -th sample within the multiple models is calculated as

$$z^{(n)}(\mathbf{x}) = W_{\text{Iwasaki}}^{(n)} z_{\text{Iwasaki}}(\mathbf{x}) + W_{\text{Slab2}}^{(n)} z_{\text{Slab2}}(\mathbf{x}) + W_{\text{Nakanishi}}^{(n)} z_{\text{Nakanishi}}(\mathbf{x}), \quad (18)$$

367
368
369
370
371
372
373
374
375
376
377

where $z^{(n)}(\mathbf{x})$, $z_{\text{Iwasaki}}(\mathbf{x})$, $z_{\text{Slab2}}(\mathbf{x})$, and $z_{\text{Nakanishi}}(\mathbf{x})$ are the z coordinates of the plate boundary geometry at the location \mathbf{x} in the horizontal plane in the n -th sample, Iwasaki model, Slab2, and Nakanishi model, respectively. $W_{\text{Iwasaki}}^{(n)}$, $W_{\text{Slab2}}^{(n)}$, and $W_{\text{Nakanishi}}^{(n)}$ are the weights of the Iwasaki, Slab2, and Nakanishi models in the n -th sample, satisfying $W_{\text{Iwasaki}}^{(n)} + W_{\text{Slab2}}^{(n)} + W_{\text{Nakanishi}}^{(n)} = 1$. We assume that the stochastic property of these weights follows the Dirichlet distribution with $\alpha_i = 1$ ($i = 1, \dots, K$), which corresponds to a uniform distribution over the $K - 1$ -dimensional simplex, where K is the number of the plate boundary geometry model considered and currently $K = 3$. Figure 4 shows a ternary plot to denote the samples from the prior PDF for the plate boundary geometry model when the ensemble size N is taken to be 2,000.

378
379
380
381
382
383
384
385
386
387
388
389
390

It is difficult to uniquely choose the material properties of the crust and mantle for the two-layered model based on published detailed elastic structure models for the target domain. Here, we assume that this room for the choice of parameters is the source of uncertainty in the underground elastic property model. We constructed a crustal model based on the Japan Integrated Velocity Structure Model (JIVSM) database (Koketsu et al., 2009, 2012). The JIVSM contains a digital elevation model for a layered seismic velocity and density structure for the region beneath the Japanese Islands, including the P-wave velocity, S-wave velocity, and density of each layer. To create an ensemble of multiple models of the crust, we focus on the structure above the Moho at the hanging wall in a region between 130.8°E and 133.6°E in the east-west direction and 32.0°N and 34.4°N in the north-south direction, within which the observation points used for the estimation for the 2010 event are located. The random samples that consist of the ensemble to model the uncer-

391 tainty of the crustal parameters are generated in the following manner, shown as
 392 two-dimensional schematics in Figure 5 (a). We randomly select N grid points in the
 393 horizontal plane from the domain. Then, we focus on the one-dimensional structure
 394 below each point and use the crustal thickness and the average elastic parameters
 395 within the crust (the layers above the Moho) as the property of the sampling point.
 396 Thus, N samples for the thickness and elastic parameters of the crust are obtained.
 397 For the properties of the mantle, we used the P-wave velocity structure model of
 398 Nakanishi et al. (2018), which includes more detailed information for spatial dis-
 399 tribution, although only P-wave velocity is included in the database. In the same
 400 manner, as for the crustal model, the average P-wave velocity from the Moho to the
 401 bottom of their model, 60 km depth, below a randomly chosen grid point is consid-
 402 ered as the elastic property for a sampling point (Figure 5 (b)). The corresponding
 403 S-wave velocity and density are set based on an empirical relation of the elastic pa-
 404 rameters in the earth (Brocher, 2005). Figure 6 shows the histogram for the ran-
 405 dom samples of elastic parameters that describes the prior PDF when the ensemble
 406 size N is taken to be 2,000. Because we focus only on static deformation, only two
 407 elastic parameters, rigidity and Poisson’s ratio for the crust and mantle, denoted by
 408 $\mu_{\text{crust}}^{(n)}$, $\nu_{\text{crust}}^{(n)}$, $\mu_{\text{mantle}}^{(n)}$, and $\nu_{\text{mantle}}^{(n)}$, respectively, are explicitly used in the analyses.

409 In total, the n -th sample of the vector for the underground structure parameter
 410 consists of eight elements:

$$\varphi^{(n)} = \{W_{\text{Iwasaki}}^{(n)}, W_{\text{Slab2}}^{(n)}, W_{\text{Nakanishi}}^{(n)}, D_{\text{crust}}^{(n)}, \mu_{\text{crust}}^{(n)}, \nu_{\text{crust}}^{(n)}, \mu_{\text{mantle}}^{(n)}, \nu_{\text{mantle}}^{(n)}\}, \quad (19)$$

411 where $D_{\text{crust}}^{(n)}$ is the crustal thickness of the n th sample. Note that some of the com-
 412 ponents in $\varphi^{(n)}$ are not necessarily independent of each other. Table 1 shows a sum-
 413 mary of the random samples for the underground structure.

414 Because it is natural to assume that the underground structure around the tar-
 415 get region does not change drastically over several years, which is a typical interval
 416 between the two sequential L-SSEs, the posterior PDF of the underground structure
 417 obtained for the 2010 L-SSE can be used as input information for the estimation of
 418 the 2018 L-SSE as the prior PDF: Following the formulations in Section 3.1, we ob-
 419 tain the posterior PDF $P(\varphi|\mathbf{d})$, which consists of the same multiple models as in the
 420 prior, while the importance weight $w^{(n)}$ on each member is updated through the slip
 421 estimation for the 2010 L-SSE. $P(\varphi|\mathbf{d})$ that we obtain here can be used as $P(\varphi)$ in
 422 Equation 3. However, the weight of many members is likely close to zero through
 423 the estimation for the 2010 event, which may lead to failure in effectively approxi-
 424 mating the posterior PDF in the next estimation. This is a problem known as “de-
 425 generacy”, which is common to ensemble-based filtering methods such as the particle
 426 filter (Gordon et al., 1993; Kitagawa, 1993, 1996). We can use the same solution as
 427 deployed in the particle filter method, that is, resampling new multiple models from
 428 the weighted samples that consist of the posterior PDF of φ obtained in the pre-
 429 vious estimation to approximate the prior PDF for the next estimation. Here, we
 430 use the most basic approach proposed in Kitagawa (1993), which performs sampling
 431 with replacement from the original samples with probabilities proportional to $w^{(n)}$.

432 3.3 Fault slip parametrization and calculation method

433 We consider a fault slip distribution at the plate boundary between 131.5°E
 434 and 133.5°E in the east-west direction, 32.15°N, and 33.9°N in the north-south di-
 435 rection and within the depth range of 0-55 km in the Nakanishi model. We expanded
 436 the slip distribution using a bilinear interpolation function. In parametrizing the
 437 slip distribution, we fix the horizontal position of the grid points that discretize the
 438 slip while considering a variety of geometric models of the plate boundary. There-
 439 fore, the depth and area of each small fault vary depending on the geometry of the
 440 model. The size of the grid spacing is an important parameter because it determines

441 the number of unknown parameters in the estimation. A proper choice of the num-
 442 ber of unknown parameters is another important factor in preventing overfitting, in
 443 addition to accurate consideration of model prediction errors. For most of the cases
 444 presented in the following section, a grid size of 16 km interval is used (Figure 7),
 445 determined based on the widely applicable Bayesian information criterion (WBIC)
 446 (Watanabe, 2013). WBIC approximates the Bayes free energy, or the minus loga-
 447 rithm of Bayes marginal likelihood, which plays an important role in a statistical
 448 model evaluation for singular statistical models (see the text in Supporting Infor-
 449 mation for details). We estimate the slip norm in each of the 130 small faults and a
 450 single rake deviation from the direction opposite to subduction, which is common to
 451 all small faults. The direction opposite to subduction is assumed to be 125° in the
 452 north-based azimuth following Heki and Miyazaki (2001). We also consider a hyper-
 453 parameter σ regarding the scaling of the observation errors, that is, we introduce a
 454 covariance matrix $\mathbf{E} = \sigma \mathbf{E}'$ into Equation 6, where the diagonal and non-diagonal
 455 components of \mathbf{E}' are taken based on the knowledge of the property of observation
 456 errors and taken to be zero, respectively. The total number of elements in \mathbf{m} in the
 457 case of a 16 km grid interval is 132.

458 The prior PDFs for the unknown parameters are based on a uniform distri-
 459 bution, which we regard as a typical weakly informative prior, as shown in Table
 460 2. While the PDFs are essentially based on a uniform distribution, we use a cosine
 461 tapered uniform distribution for the prior PDF for slip distribution, which is charac-
 462 terized by four numbers a', a, b, b' , where $a' \leq a \leq b \leq b'$. The probability density
 463 is uniformly distributed in the range between a and b , whereas the edge of the dis-
 464 tribution is tapered using a cosine curve in the range between a' and a , and b and b'
 465 (see Appendix B for details). Such tapered uniform distribution is often used when
 466 a high probability of a parameter is expected near the edge of the uniform distribu-
 467 tion in the posterior PDF. An estimation of slip distribution can be a typical exam-
 468 ple of such a case. The prior PDF for non-negative constraint is often used, while
 469 it is natural to expect that the amount of slip in many of the small faults tends to
 470 be nearly zero. We use a cosine taper only for the lower edge of the distribution, in
 471 the range between -0.1 m and 0 m. The lower limit -0.1 m is chosen as a limit of back
 472 slip allowed based on the Nankai Trough subduction zone, in which the convergence
 473 rate is estimated to be around 0.06 m/year (Heki & Miyazaki, 2001). Since the tar-
 474 get period for the processed GNSS data for the 2010 L-SSE is 1.7 years, 0.1 m (\simeq
 475 0.06 m/year \times 1.7 years) is used as the lower limit. Although the target period for
 476 the 2018 L-SSE is shorter (0.6 years), the same prior PDF is used for this event for
 477 ease of comparison with the 2010 L-SSE.

478 2,000 sets of the response function to each of the input unit fault slip in the di-
 479 rection of subduction and one perpendicular to it are calculated using EDGRN/EDCMP
 480 (Wang et al., 2003). Each set corresponds to the matrix $\mathbf{G}(\varphi)$ in Equation 6. In
 481 each iteration of the REMC sampling, these response functions in the two directions
 482 are superimposed according to the slip norm in each fault and the common rake de-
 483 viation given in \mathbf{m} in the current sampling step.

484 To draw samples from the posterior PDF using the REMC method, we took
 485 replicas $L = 32$ (and 48 for some cases depending on the setting). We take 150,000
 486 burn-in steps and 350,000 sampling steps. Replica exchange is performed once in ev-
 487 ery five steps between two randomly selected replicas. We output a sample in every
 488 50 steps to avoid taking strongly correlated samples. Because the algorithm requires
 489 the calculation of $\mathbf{G}(\varphi)\mathbf{m}$ in Equation 6 for each $\varphi^{(n)}$ at every time step, proper ac-
 490 celeration is necessary. We accelerate the sampling calculation using multi-GPGPU
 491 (i.e., general-purpose computing on graphics processing units), assigning a GPU
 492 to the calculation for every replica. The use of 16 NVIDIA A100 GPUs, installed

493 in Earth Simulator 4 at Japan Agency for Marine-Earth Science and Technology
 494 (JAMSTEC), allows sampling to be completed within less than an hour.

495 3.4 Numerical experiment

496 We present numerical experiments in a problem setting that mimics the actual
 497 estimation problem described in the next section. We used artificial data calculated
 498 based on the true fault slip and underground structure and applied BMMFSE to
 499 the estimation of both the slip and the structure based on the prior PDF for the un-
 500 derground structure introduced in the previous subsections. We consider two true
 501 slip models, SM_{sharp} and SM_{smooth} : The former exhibits a discontinuous change in
 502 the slip distribution, and the latter has a smooth distribution in the entire region
 503 (Figure 8 (a) and (d)). We investigate how BMMFSE and a conventional method,
 504 which is based on a single underground structure model and a strong prior con-
 505 straint based on a discretized Laplacian operator to impose smoothness on the slip
 506 distribution (explained in detail later), estimate the slip distribution for the two
 507 models. The true underground structure model assumed here is given by the aver-
 508 age of the two plate boundary geometry models, Slab2 and the Iwasaki model (i.e.,
 509 $W_{\text{Iwasaki}} = 0.5$, $W_{\text{Slab2}} = 0.5$, and $W_{\text{Nakanishi}} = 0$), and elastic parameters presented
 510 in Table 3. The response displacement is calculated based on these true models. We
 511 added artificial Gaussian noise to the calculated displacements, for which the stan-
 512 dard deviations were 2×10^{-3} m for the horizontal component and 6×10^{-3} m for the
 513 vertical component, following the error level presented in Yoshioka et al. (2015). \mathbf{E}'
 514 is obtained according to this standard deviation setting.

515 The estimated fault slips using BMMFSE are shown in Figure 8. The mean
 516 slip distribution ((b) for SM_{sharp} and (e) for SM_{smooth}) implies that the proposed
 517 method can distinguish the tight and broad distributions in SM_{sharp} and SM_{smooth} ,
 518 respectively. However, because BMMFSE estimates non-Gaussian posterior PDFs,
 519 solely mean values are not sufficient. Figure 8 (c) and (f) shows frequency plot of
 520 slips in the MCMC samples along the A-B line marked in (a), (b), (d) and (e). Be-
 521 cause the region with large slips, which spans from 60 to 120 km away from Point
 522 A, is mostly beneath the Bungo Channel and lacks observation stations above, esti-
 523 mation uncertainty is relatively large. On the other hand, the overall distribution of
 524 the estimated frequency was consistent with the true slip distribution in both mod-
 525 els. Figure 9 shows the plots for the posterior PDF for the underground structure
 526 for the SM_{sharp} . For the parameters of the plate boundary geometry (Figure 9 (a)
 527 and (b)), W_{Slab2} is distributed around 0.5, and W_{Iwasaki} and $W_{\text{Nakanishi}}$ have a simi-
 528 lar distribution to that of each other, although the probability density near the point
 529 representing the true model appears to be slightly large. These findings suggest that
 530 the data cannot clearly distinguish the weights of the Iwasaki and Nakanishi models,
 531 while the true model is estimated to be nearly an average of Slab2 and a weighted
 532 average of the two models. This is reasonable because the Iwasaki and Nakanishi
 533 models are far closer to each other than Slab2, as shown in Figure 3. The estima-
 534 tion result for the plate boundary in SM_{smooth} shows the same tendency (Figure S1).
 535 In the estimation of the elastic parameters (Figure 9 (c) and (d)), no strong peak
 536 is estimated in the bin for the true values in the histograms. In the crust, relatively
 537 strong peaks observed in the prior distribution disappear in the posterior distribu-
 538 tion. It appears that the data are insensitive to the parameters for the mantle be-
 539 cause the prior and posterior do not have significant differences.

540 For comparison, we also performed an estimation using a conventional method,
 541 including a certain amount of model prediction errors. We use the Nakanishi model
 542 for the plate boundary geometry assuming a homogeneous elastic half-space with
 543 $\nu = 0.25$, which is one of the most widely used settings of the elastic property in
 544 slip inversion using geodetic data. The conventional method we consider here uses

545 a strong prior constraint based on a finite-difference approximation of the Lapla-
 546 cian operator for the smoothness of the slip distribution, which we hereafter call the
 547 “smoothing” model. The smoothing model is taken with a Bayesian model with a
 548 prior constraint on the smoothness with unknown hyperparameters, which is deter-
 549 mined using an information criterion (Yabuki & Matsu’ura, 1992). The estimated
 550 slip distributions of SM_{sharp} and SM_{smooth} on the A-B line are shown in Figure 8 (c)
 551 and (f), respectively. Due to the smoothness constraints, relatively smooth distri-
 552 butions are obtained not only for SM_{smooth} but also for SM_{sharp} . In particular, the
 553 slip distribution on the down-dip side of the channel (approximately 120 to 150 km
 554 from Point A), for which SM_{sharp} and SM_{smooth} have a steep and smooth variation,
 555 respectively, are estimated to be similar smooth variations for both models. Thus,
 556 the introduction of a smoothness constraint may lead to difficulty in distinguishing
 557 the sharpness of the slip distribution at the down-dip side of the channel, unlike the
 558 estimates using BMMFSE.

559 4 Posterior PDF of slip distribution and underground structure 560 based on the geodetic data for the L-SSEs occurring beneath 561 the Bungo Channel around 2010 and 2018

562 4.1 Posterior PDF for slip distribution

563 Figure 10 shows an overview of the posterior PDF for the slip distribution
 564 $P(\mathbf{m}|\mathbf{d})$ estimated for the 2010 L-SSE. The mean model of the posterior PDF of
 565 \mathbf{m} is plotted in Figure 10 (a). The main rupture area with a mean slip larger than
 566 0.1 m is estimated to occur in a relatively narrow region in the north-south direc-
 567 tion. The mean of the predictive PDF for the displacement (see Appendix C for the
 568 definition of the predictive PDF) agrees well with the observation data (Figure 10
 569 (b)(c)) and is not associated with a significant systematic residual distribution (Fig-
 570 ure S2 (a)(b)). However, because the posterior PDF of \mathbf{m} has a non-Gaussian fea-
 571 ture, only paying attention to the mean model may be misleading in understanding
 572 the features of the posterior PDF. Figure 10 (d) shows the normalized frequency of
 573 sampled slip parameter on the line from A to B marked in (a) and the histograms
 574 of slips in selected small faults. The amount of slip in the dip direction in the re-
 575 gion between approximately 60 km and 120 km from Point A (e.g., (ii) in Figure 10
 576 (d)), which corresponds to the area directly beneath the Bungo channel, has a large
 577 variation, while those elsewhere have significantly large frequencies around the bin
 578 of 0 m slip (e.g., (i) and (iii) in Figure 10 (d)). This contrast clearly reflects the ef-
 579 fect of the absence of observation points in the channel. The rake deviation of the
 580 slip from the direction opposite to subduction (i.e., 125° in the north-based azimuth)
 581 in the counter-clockwise direction was estimated to be approximately five degrees
 582 with a standard deviation of approximately one degree, which corresponds to a slip
 583 direction of approximately 120° azimuth. These results are consistent with the slip
 584 direction estimated for the fault patches with large slip amounts by Yoshioka et al.
 585 (2015) (see Figure S3 and the text in Supporting Information).

586 The histograms of slips in (i), (ii), and (iii) show asymmetric distribution shapes.
 587 This non-Gaussian feature of the marginal posterior PDF for the estimated slip sug-
 588 gests that the use of standard deviation may be inappropriate for quantifying the
 589 estimation uncertainty. Instead, we calculate the information gain before the poste-
 590 rior marginal PDFs based on the following definition:

$$IG_i = \int_{-\infty}^{\infty} P(m_i|\mathbf{d}) \log_2 \frac{P(m_i|\mathbf{d})}{P(m_i)} dm_i, \quad (20)$$

591 where IG_i and m_i are the information gain, whose unit is bit here, and the slip
 592 amount in the i -th small fault, respectively. The PDF regarding m_i here is marginal-
 593 ized. Information gain is also known as the Kullback-Leibler divergence, which quan-

594 tifies the difference between two PDFs. The integration and density $P(m_i|\mathbf{d})$ in
 595 Equation 20 are evaluated approximately by using the Monte Carlo integration and
 596 kernel density estimation based on the REMC samples, respectively. Figure 10 (e)
 597 shows a plot of the information gain for each small fault via the estimation for the
 598 2010 event. Information gain is relatively small, not only in the small faults at the
 599 northern and southernmost parts, which are distant from the locations of the ob-
 600 servation points but also in those beneath the Bungo Channel, around which the
 601 largest mean slip is estimated.

602 We also calculated the PDF for the seismic moment release following the defi-
 603 nition of the predictive PDF. Fault slip at small faults with a small information gain
 604 should not be considered when calculating the seismic moment release. Otherwise,
 605 the prior PDF for the slip amount, which is characterized by a uniform distribution
 606 between 0 and 1 m, may have a substantial impact and lead to a significant bias in
 607 seismic moment estimation, that is, the mean model of the prior PDF for slip results
 608 in a uniform slip of 0.5 m, which corresponds to nearly M_w 8, an unrealistically large
 609 value for an L-SSE. Although there is no objective criterion for this information-gain
 610 threshold to calculate the seismic moment, the resulting seismic moment releases M_o
 611 falls in the same order as those estimated in previous studies when $IG = 1.5$ is used
 612 as the information gain threshold, that is, $(2.74 \pm 0.57) \times 10^{19}$ N m, which corresponds
 613 to M_w 6.89 ± 0.06 , where the number following \pm corresponds to a $2\text{-}\sigma$ value. $IG = 0$
 614 results in significantly larger M_o and M_w than those estimated in previous studies
 615 (Table 4). Note that the mean and standard deviation values do not satisfy the re-
 616 lation of and M_w because we calculated the statistics for M_w based on the random
 617 samples, for each of which we converted M_o to M_w using the relation. In addition,
 618 it is not straightforward to perform a fair comparison of seismic moment release es-
 619 timated by employing widely used approaches and a Bayesian estimation scheme
 620 based on a weakly informative prior, as indicated by the above discussion.

621 Figure 11 shows the overview of the posterior PDF for slip distribution $P(\mathbf{m}|\mathbf{d})$
 622 in the 2018 L-SSE. The main rupture area of the mean slip distribution is seen in
 623 a similar location but with a relatively small amount of slip compared to that of
 624 the estimate for the 2010 event (Figure 11 (a)). As in the case of the 2010 L-SSE,
 625 the mean of the predictive PDF for the displacement agrees well with the observa-
 626 tion data (Figure 11 (b)(c)). The systematic residual distribution is not significant
 627 except for the southern part of Kyushu Island (stations located at around 32°N)
 628 (Figure S2 (c)(d)), which is unlikely to have a significant impact on the estimation
 629 results for the main rupture area. Although there is a significant amount of uncer-
 630 tainty, the 2018 L-SSE is likely to have hosted a smaller moment release, for exam-
 631 ple, $(2.35 \pm 0.51) \times 10^{19}$ N m, which corresponds to M_w 6.84 ± 0.07 , when $IG = 1.5$
 632 is adopted. This relationship is reasonable because the event duration we focus on in
 633 this study was significantly shorter in the 2018 L-SSE. However, the normalized fre-
 634 quency of the sampled slip parameter on the cross line from A to B shows a similar
 635 feature to that in the 2010 event, suggesting that these events are similar in terms
 636 of the up- and down-dip limits of the slip distribution (Figure 11 (d)). Similar to
 637 the 2010 L-SSE, the rake deviation of the slip from the direction opposite to subduc-
 638 tion (i.e., 125° in the north-based azimuth) was estimated to be approximately five
 639 degrees with a standard deviation of approximately one degree. As a result, the his-
 640 togram for the slip direction estimated for the 2018 L-SSE shows a similar pattern
 641 to that of the one in 2010 (Figure S3).

642 4.2 Posterior PDF for underground structure

643 Figure 12 (b) shows the ternary plots for the posterior PDF for the plate bound-
 644 ary geometry models obtained in the estimation for the 2010 L-SSE. The small tri-
 645 angles corresponding to $0.3 \leq W_{\text{slab2}} \leq 0.6$ have frequencies that are approximately

646 five times higher at maximum than the average frequency in the ternary plot for the
 647 prior PDFs shown again in Figure 12 (a). This pattern indicates that the geodetic
 648 dataset prefers an intermediate plate boundary model between Slab2 and a mixture
 649 of the Iwasaki and Nakanishi models. On the other hand, these small triangles with
 650 a high frequency do not have strong contrast in terms of the values of W_{Iwasaki} and
 651 $W_{\text{Nakanishi}}$, which suggests that the dataset does not clearly distinguish between the
 652 contributions of the Iwasaki and Nakanishi models, similar to the results of the nu-
 653 merical experiment presented in Section 3.4. In contrast, the histograms for the pos-
 654 terior PDF for the elastic structure do not change significantly from those for the
 655 prior, with an increase in frequency at a maximum of approximately twice in each
 656 bin of the histograms (Figure 13 (b)). These results are consistent with previous re-
 657 ports that the choice of plate boundary model often has a larger impact on the esti-
 658 mation results than that of the elastic structure in estimating slip distribution using
 659 geodetic data (e.g., Lindsey and Fialko (2013); Li and Barnhart (2020)).

660 The weighted samples visualized in Figure 12 (b) and Figure 13 (b) are resam-
 661 pled using the approach explained in Section 3.2 to generate the new ensembles of
 662 the underground structure models used as the input for the estimation of the 2018
 663 L-SSE. The ternary plot and the histograms for the new samples (Figure S4) are al-
 664 most identical to those presented in Figure 12 (b) and Figure 13 (b). Figure 12 (c)
 665 and 13 (c) show the ternary plots and the histogram for the posterior PDF for the
 666 plate boundary geometry and the elastic structure model, respectively, obtained in
 667 the estimation for the 2018 L-SSE. The basic feature in the obtained posterior PDFs
 668 is the same as in the estimation results for the 2010 L-SSE, with further higher fre-
 669 quencies in the triangles corresponding to $0.4 \leq W_{\text{Slab2}} \leq 0.6$ for the posterior PDF
 670 of the plate boundary geometry model.

671 5 Discussion

672 5.1 Comparison of up- and down-dip limit of slip distribution with 673 methods based on stronger prior constraints

674 We compare the estimation results obtained by using BMMFSE with those
 675 obtained using two previous methods based on strong prior constraints. One is the
 676 smoothing model, which was also used in the numerical experiments in Section 3.4.
 677 The Nakanishi model and an elastic half-space with $\nu = 0.25$ were used as the plate
 678 boundary model and elastic structure, following the setting of the numerical exper-
 679 iments. The other is a fused lasso model, which is obtained by using a fused lasso
 680 method (Tibshirani et al., 2005), which promotes both sparsity and smoothness
 681 of the parameter distribution using L1-norm-based penalization. We use the result
 682 from Nakata et al. (2017), who applied this method to L-SSEs in the Bungo Channel
 683 aiming at detecting discontinuous changes in the slip distribution, as the fused lasso
 684 model. The fused lasso model is only available for the 2010 L-SSE and is also based
 685 on an elastic half-space with $\nu = 0.25$ but uses a different plate boundary geometry
 686 model based on Baba et al. (2002).

687 Figure 14 (a) and (c) show the comparison of slip estimation results for the
 688 2010 and 2018 L-SSE obtained by using BMMFSE and the previous methods. The
 689 slip profile at the up-dip side of the main rupture area in the three models (denoted
 690 by the orange double-headed arrows in (a) and (c)) agrees well with each other in
 691 the 2010 L-SSE and the two models in the 2018 L-SSE. On the other hand, we found
 692 significant variations at the down-dip side. In the 2010 L-SSE, at the location where
 693 the slope of the slip distribution at the down-dip side starts (denoted by the cyan
 694 double-headed arrow only in (a)), while the mean models of BMMFSE and the fused
 695 lasso model agree well in terms of the slope, the smoothing model shows a slightly
 696 larger amount of slip than in the others. In the location further from A (denoted

697 by the pink double-headed arrow in (a) and (c)), we observe a moderate slope in
 698 the slip distribution of the smoothing model in contrast to the steep one seen in
 699 BMMFSE. This feature of difference is even clearer in the 2018 L-SSE. We observed
 700 similar differences at the down-dip side in the comparison between the BMMFSE
 701 and the smoothing model in the numerical experiment presented in Section 3.4.
 702 Therefore, it is likely that this moderate slope in the smoothing model is an arti-
 703 fact introduced owing to the use of a strong prior constraint and an underground
 704 structure that is likely to have introduced a significant amount of model prediction
 705 errors. The fused lasso model exhibits a large amount of slip with a flat distribution
 706 shape owing to the L1-norm-based penalty on the smoothness in the area of the pink
 707 double arrows. The histograms of the slip amount on line (i) shown in Figure 10 (d)
 708 and 11 (d) estimated by BMMFSE in a patch within this down-dip region suggest
 709 that the posterior PDF indeed permits a larger amount of slip, but the probability
 710 for such cases is not very high, according to our analyses.

711 During the period of both L-SSEs, a number of deep tremors synchronously
 712 occurred at the down-dip side of the main rupture region (the white bars in Figure
 713 14), the number of which increased compared to the period before the L-SSEs (see
 714 Figure S5 and note that the occurrence of surrounding S-SSEs reported by Kano
 715 et al. (2019) is considered when counting the number of tremors). Although there
 716 seems to be a correspondence between the estimated slope of the slip distributions
 717 at the down-dip side and the distribution of the number of tremors, further discus-
 718 sion is difficult if only based on this information. Therefore, we calculate the change
 719 in the Coulomb failure stress (ΔCFS) because of the estimated slip during the L-
 720 SSE period using an analytical expression of elastic deformation in a homogeneous
 721 half-space (Comninou & Dundurs, 1975). We use a simple form for calculating the
 722 change as

$$\Delta\text{CFS} = \Delta\tau + f\Delta\sigma_n \quad (21)$$

723 where $\Delta\tau$ is the shear stress change on the fault, f is the effective friction coeffi-
 724 cient, and $\Delta\sigma_n$ is the normal stress change with the expanding direction as positive.
 725 The direction for shear stress is taken to be the opposite of the subduction. We only
 726 calculated ΔCFS for the estimation results of BMMFSE and the smoothing model
 727 because the fused lasso model, which allows abrupt changes in the spatial distribu-
 728 tion of the parameters, is not suitable for calculating the shear stress on the fault.
 729 Note that efforts have also been made to introduce a prior constraint that combines
 730 the distribution of smoother variations globally and abrupt changes locally in the
 731 framework of the fused lasso method (Nakata et al., 2016). We present the result
 732 assuming $f = 0.2$ for both models, reflecting an estimation result for a relatively
 733 low friction coefficient in the deep fault (Houston, 2015). For BMMFSE, the elastic
 734 half-space with Poisson's ratio of the elastic parameter of the mantle layer is used to
 735 calculate the shear and normal stresses.

736 Figure 14 (b) and (d) compare ΔCFS calculated based on the slip distribution
 737 obtained using BMMFSE and that of the smoothing model for the 2010 and 2018
 738 L-SSE, respectively. In both events, the location of the peak of the positive value
 739 of the mean ΔCFS in the down-dip side of the channel for BMMFSE (denoted by
 740 the red star in (b) and (d)) is consistent with the bin with the largest number of
 741 tectonic tremors during the L-SSE period. On the other hand, the location of the
 742 corresponding peak in the smoothing model is not very consistent with that of the
 743 tremor distribution in the 2010 L-SSE, and such a peak with a positive ΔCFS is in-
 744 significant in the 2018 L-SSE (denoted by the green star). Moreover, BMMFSE es-
 745 timates a steeper slip distribution in the down-dip for the 2018 L-SSE, which results
 746 in a narrower region along the line for positive ΔCFS , compared to those for the
 747 2010 one (see the gray double-headed arrows in (b) and (d)). This contrast of the
 748 broad and narrow region of positive ΔCFS appears to agree to the spatial change of

749 tremors: the number of tremors during the 2018 L-SSE abruptly decreases from the
 750 first bin to the second bin from the side of Point A, which is in contrast to the more
 751 moderate decrease seen in the 2010 one. Such possible correspondences are blurred
 752 in the smoothing model. These contrasts between the two methods are observed ro-
 753 bustly for different assumptions of f , indicated by the distribution of $\Delta\sigma_n$ and $\Delta\tau$
 754 (Figure S6), although we need to note that the uncertainty is that the calculated
 755 stresses are not small.

756 The correspondence between the spatial distribution of ΔCFS and tremors in
 757 the estimation results obtained using BMMFSE implies a direct mechanical rela-
 758 tionship between slip in L-SSE and triggering of tremors. The mechanism of syn-
 759 chronization of L-SSE and tremors, which has also been observed in other subduc-
 760 tion zones in the world, has remained controversial. For instance, for a similar syn-
 761 chronization known in the Guerrero subduction zone in Mexico, Kostoglodov et al.
 762 (2010) and Frank et al. (2015) attributed the synchronization to the increase in
 763 shear stress owing to L-SSE, while Villafuerte and Cruz-Atienza (2017) suggested
 764 that the stress concentration on the rupture front of the SSE owing to the increase
 765 in slip rate increased the number of tremors as the main mechanism. The results
 766 we obtain here seem consistent with the former mechanism. Of course, because we
 767 only focus on the total slip distribution during the L-SSE period, detailed discus-
 768 sion requires investigation of spatio-temporal evolution, such as that performed in
 769 Villafuerte and Cruz-Atienza (2017). Nevertheless, our results suggest that estima-
 770 tion of slip distribution with and without introducing strong prior constraints may
 771 lead to a qualitatively different conclusion on the synchronization of SSEs and sur-
 772 rounding slow earthquakes. For example, the slip distribution models adopted in
 773 the studies on L-SSEs in the Guerrero subduction zone referred to above were based
 774 on fault slip estimation using smoothing constraints. Therefore, the effects of these
 775 constraints on their discussion should be studied further. Bartlow et al. (2011) con-
 776 sidered the relationship between S-SSE and tremors in the Cascadia subduction zone
 777 in North America, taking into consideration the impact of the smoothing filter in
 778 estimating the slip distribution of SSE suggested by numerical experiments. Fault
 779 slip estimation incorporating only weakly informative prior PDFs, as performed in
 780 this study, can be a more direct solution to the possible confusion brought about by
 781 adopting strong prior constraints.

782 5.2 Underground structure models preferred by the geodetic data

783 It is understandable to expect that either the Iwasaki or the Nakanishi model
 784 represents well the true plate boundary geometry in the target region because these
 785 two models were constructed based on the combination of more local information
 786 than that used in Slab2, in which global data were more emphasized. For instance,
 787 the Nakanishi model combines information from seismic surveys for shallower and
 788 microseismicity for the deeper portion of the plate boundary. However, as shown
 789 in Section 4.2 and Figure 12 (b) and (c), the posterior PDF for the plate bound-
 790 ary model we obtained has a large frequency for the intermediate models between
 791 Slab2 and the mixture of the others. The depth of Slab2 is significantly larger than
 792 that of the Iwasaki and Nakanishi models, while those of the latter two models are
 793 relatively similar in most parts of the target region, as shown in Figure 3. There-
 794 fore, the depth of the group of the plate boundary models preferred by the data in
 795 our estimation is generally larger than those in the Iwasaki and Nakanishi models.
 796 On the other hand, the estimated plate boundary geometry in this study has a cer-
 797 tain amount of uncertainty; for example, the model with the weights denoted by the
 798 pink and magenta circles in Figure 12 (a), (b), and (c) is associated with equally
 799 high probability in both the estimation for the 2010 and 2018 L-SSE. The plot of
 800 the resulting plate boundary models compared with the original three models in
 801 Figure 12 (d) shows that the difference in the model denoted by the pink color is

802 within a few kilometers from the Nakanishi model at a depth range of approximately
 803 30 km, where a large portion of slip is likely to take place. In the deeper portion of
 804 the Nakanishi model, the top of the hypocenter locations determined by seismic to-
 805 mography analyses was chosen as the trace of the plate boundary (Yamamoto et al.,
 806 2013). Therefore, this small difference may be within the uncertainty of hypocenter
 807 locations. We also should note that our evaluation does not apply to the entire do-
 808 main of each fault geometry model because the geodetic data we used here contain
 809 the information of the geometry only within a small portion of the domain.

810 In the estimation for the 2010 L-SSE, the relatively tall bins seen in the his-
 811 tograms for prior PDF for the crustal thickness and elastic parameters become un-
 812 noticeable in the posterior PDF: Despite these characteristic priors, the data suggest
 813 that it is difficult to constrain the details of the crustal layer using the geodetic data.
 814 One of the possible reasons for the large uncertainty in the posterior PDF for the
 815 crustal model is that the data cannot resolve the slips in the shallow portion of the
 816 fault plane well, which should be more strongly related to the shallow layers. The
 817 portion of the fault plane in which relatively large slips are estimated tends to be
 818 located deeper than the lower limit of the crustal layer.

819 Both the results for the 2010 and 2018 L-SSE, the histogram for the posterior
 820 PDF of the elastic parameters in the mantle layer has the highest frequency in the
 821 bins at the lower bound, which are taller than in the prior PDF. This finding im-
 822 plies that the insertion of another layer corresponding to the lower crust, for which
 823 it is natural to assume smaller rigidity and larger Poisson's ratio than in the mantle
 824 layer, to the two-layered elastic structure is a possible improvement for the present
 825 model setting. However, this improvement is beyond the scope of this study, because
 826 we assume that the insertion of another layer does not significantly affect the estima-
 827 tion results for slip distribution.

828 **5.3 Effect of updating underground structure through sequential es-** 829 **timation of L-SSE**

830 In the estimation for the 2018 L-SSE, the posterior PDF of the underground
 831 structure obtained for the 2010 L-SSE was used as the prior PDF. To see how in-
 832 corporating the PDF for the underground structure updated through the estima-
 833 tion for the 2010 L-SSE affects the results of the 2018 L-SSE, we show the estima-
 834 tion result for 2018 using the original prior PDF (Figure 4 and 6) directly in Figure
 835 15. Comparing this with the results shown in Figure 11, we do not observe a signifi-
 836 cant difference in the slip distribution. We observed almost the same features in the
 837 posterior PDF for the underground structure. In general, the proper choice of prior
 838 PDFs contributes to the avoidance of overfitting in an estimation. The similarity be-
 839 tween the result for the 2018 L-SSE with and without the PDF for the underground
 840 structure obtained for that of 2010 implies that the original prior PDF for the un-
 841 derground structure constructed based on the published databases is sufficient to
 842 avoid overfitting. However, the posterior PDF of the plate boundary geometry in the
 843 result based on the original prior PDF has a smoother distribution with less concen-
 844 tration of frequencies than in the result based on the prior PDF obtained from the
 845 2010 L-SSE. Noting that the 2010 L-SSE is likely to have hosted a broader slip re-
 846 gion with larger seismic moment release than the 2018 event, it is natural that more
 847 information on the plate boundary geometry is included in the prior PDF from the
 848 2010 estimation, which contributed to the reduction of the uncertainty of the poste-
 849 rior PDF. In addition, combination with the results from the preceding L-SSEs (i.e.,
 850 The events that occurred in around 1997 and 2003) may also increase the accuracy
 851 of the estimation, because the region with large slip amounts estimated in previous
 852 studies (e.g., Yoshioka et al. (2015)) are slightly different from each other.

853 WBIC of the two estimations for the 2018 L-SSE with and without the prior
 854 PDF based on that for the 2010 one are -1521.54 and -1519.14, respectively. The
 855 difference of logarithmic marginal likelihood that is larger than two corresponds to
 856 “decisive” evidence in favor of the former model (Kass & Raftery, 1995). These facts
 857 quantitatively support the idea that updating the underground structure in a se-
 858 quential estimation of L-SSEs allows for a more preferable Bayesian inference.

859 5.4 Future perspectives

860 In this study, we targeted the L-SSE in the Bungo Channel because multiple
 861 types of strong prior constraints have been applied in previous studies. In addition,
 862 the feature of the L-SSE that the events with fault slip that are detectable by the
 863 GNSS observation have repeatedly occurred in the same location is another impor-
 864 tant reason. However, we expect that fault slip estimation using the BMMFSE also
 865 provides insightful results for ordinary earthquakes. Although we focused on the es-
 866 timation using a weakly informative prior PDF for the slip distribution, the accu-
 867 rate consideration of model uncertainty that the method allows for should also be
 868 effective in estimations introducing strong prior PDFs. Moreover, by taking a fully
 869 Bayesian approach, the method can be flexibly combined with not only the widely
 870 used constraints such as the smoothing approach but also recently proposed sophis-
 871 ticated implicit (e.g., trans-dimensional inversion (Dettmer et al., 2014)) and explicit
 872 (e.g., von Karman regularization (Amey et al., 2018, 2019)) regularization schemes,
 873 which is expected to increase the quality of estimation. The probability models that
 874 were used to generate the ensemble of multiple models for the underground struc-
 875 ture were constructed in a relatively ad hoc manner in this study. The construction
 876 of a multi-model ensemble focusing on the genuine estimation errors of underground
 877 structure models is an important task in future work.

878 6 Conclusion

879 We estimated the slip distribution in the L-SSEs that occurred beneath the
 880 Bungo Channel in southwest Japan in around 2010 and 2018 using BMMFSE, a
 881 Bayesian multi-model fault slip estimation method. We performed the estimations
 882 using only weakly informative prior PDFs, such as uniform distribution instead of
 883 strong priors, by taking advantage of the accurate consideration of the model un-
 884 certainty for underground structures in BMMFSE. We use the term “strong priors”
 885 here to denote prior information on the characteristic of the slip distribution, such
 886 as smoothness, sparseness, and so on, which is incorporated to regularize the inverse
 887 problem. We constructed an ensemble of multiple models that represent the model
 888 uncertainty of underground structures as a combination of the mixture of currently
 889 published plate boundary geometry models (i.e., the Iwasaki model, Slab2, and the
 890 Nakanishi model) and two-layered elastic media based on published databases of a
 891 3D elastic structure. The posterior PDF estimated for both the 2010 and 2018 L-
 892 SSEs presents a large probability for slip models with a narrow area for the main
 893 rupture along the line in the north-south direction. Compared with the estimation
 894 results obtained by using the previous methods based on strong prior constraints,
 895 we found significant differences in the fault slip profiles at the down-dip side of the
 896 main rupture area immediately beneath the Bungo Channel. A comparison of the
 897 Coulomb failure stress change (Δ CFS) calculated based on the estimated slip distri-
 898 bution suggests that the spatial distribution of the area with positive Δ CFS agrees
 899 better with that of deep tectonic tremors that synchronously occurred during the
 900 period of the L-SSE. Moreover, the difference of the shape of the area with posi-
 901 tive Δ CFS in for the 2010 and 2018 L-SSE calculated in BMMFSE may correspond
 902 to the contrast of the spatial distribution of the number of tremors that occurred
 903 in each event. The other advantage of BMMFSE, which should match the estima-

904 tion for L-SSE, is that it can renew the posterior PDF of the underground struc-
905 ture through the estimation for each event. The posterior PDF for the underground
906 structure estimated for the 2010 L-SSE suggests that the geodetic data prefer inter-
907 mediate models between Slab2 and a mixture of the Iwasaki and Nakanishi models,
908 and the data cannot distinguish the latter two models clearly. On the other hand,
909 we did not find a strong preference for any of the multiple models of elastic structure
910 through the estimation. The choice of the plate boundary geometry model likely is
911 one of the main factors that cause model prediction errors. In the estimation for the
912 2018 L-SSE, the posterior PDF of the underground structure obtained for the 2010
913 one was used as the prior PDF. Such treatment results in a more precise estimation
914 of the plate boundary geometry than in an estimation using the same prior PDF of
915 underground structure as used in the estimation for 2010. A comparison of these
916 two estimations with different prior PDFs in terms of an information criterion also
917 suggests that the estimation using the renewed prior PDF results in a more prefer-
918 able Bayesian inference.

Table 1. An example of a set of random samples for the underground structure consisting of 2,000 members. n is the index of the samples. The units of D and μ are km and GPa, respectively.

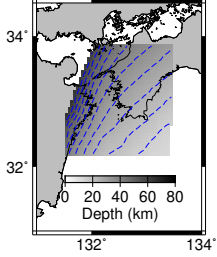
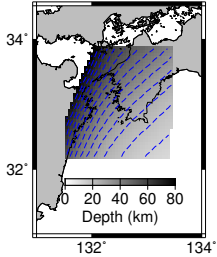
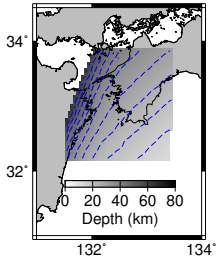
n	Plate boundary geometry	Elastic structure
1		$D_{\text{crust}}^{(1)} = 32.7$ $\mu_{\text{crust}}^{(1)} = 33.8$ $\nu_{\text{crust}}^{(1)} = 0.235$ $\mu_{\text{mantle}}^{(1)} = 63.2$ $\nu_{\text{mantle}}^{(1)} = 0.258$
⋮	⋮	⋮
401		$D_{\text{crust}}^{(401)} = 31.7$ $\mu_{\text{crust}}^{(401)} = 34.4$ $\nu_{\text{crust}}^{(401)} = 0.235$ $\mu_{\text{mantle}}^{(401)} = 60.7$ $\nu_{\text{mantle}}^{(401)} = 0.260$
⋮	⋮	⋮
2,000		$D_{\text{crust}}^{(2,000)} = 36.2$ $\mu_{\text{crust}}^{(2,000)} = 34.9$ $\nu_{\text{crust}}^{(2,000)} = 0.234$ $\mu_{\text{mantle}}^{(2,000)} = 56.1$ $\nu_{\text{mantle}}^{(2,000)} = 0.262$

Table 2. The prior PDF for the unknown parameters. $U_{\cos}(a', a, b, b')$ denotes a cosine tapered uniform distribution, where the probability density is uniformly distributed in the range between a and b , while the edge of the distribution is tapered using a cosine curve in the range between a' and a , and b and b' (see Appendix B for details). $U(a, b)$ denotes a uniform probability distribution from a to b , where $a < b$. b_σ is a sufficiently large value, which is set to three in our computation program.

	Slip norm	Rake deviation	Scale factor for observation errors
Prior PDF	$s_i \sim U_{\cos}(-0.1 \text{ m}, 0 \text{ m}, 1 \text{ m}, 1 \text{ m})$	$\Delta\lambda \sim U(-20^\circ, 20^\circ)$	$\sigma \sim U(1, b_\sigma)$

Table 3. Elastic parameters for the true underground structure model assumed in the numerical experiments.

D_{crust} (km)	μ_{crust} (GPa)	ν_{crust}	μ_{mantle} (GPa)	ν_{mantle}
23.0	31.2	0.238	62.0	0.258

Table 4. Seismic moment release (M_o) and corresponding moment magnitude (M_w) for estimated slip distribution in this study and previous ones. Note that the mean and standard deviation values do not satisfy the relation of M_o and M_w because we calculated the statistics for M_w based on the random samples, for each of which we converted M_o to M_w using the relation.

	2010 L-SSE				2018 L-SSE	
	This study		Yoshioka et al. (2015)	Nakata et al. (2017)	This study	
<i>IG</i> threshold	0	1.5	-	-	0	1.5
M_o (10^{19}N m)	6.98±0.69	2.74±0.57	2.2	-	5.82±0.52	2.35±0.51
M_w	7.16±0.03	6.89±0.06	6.8	6.9	7.11±0.03	6.84±0.05

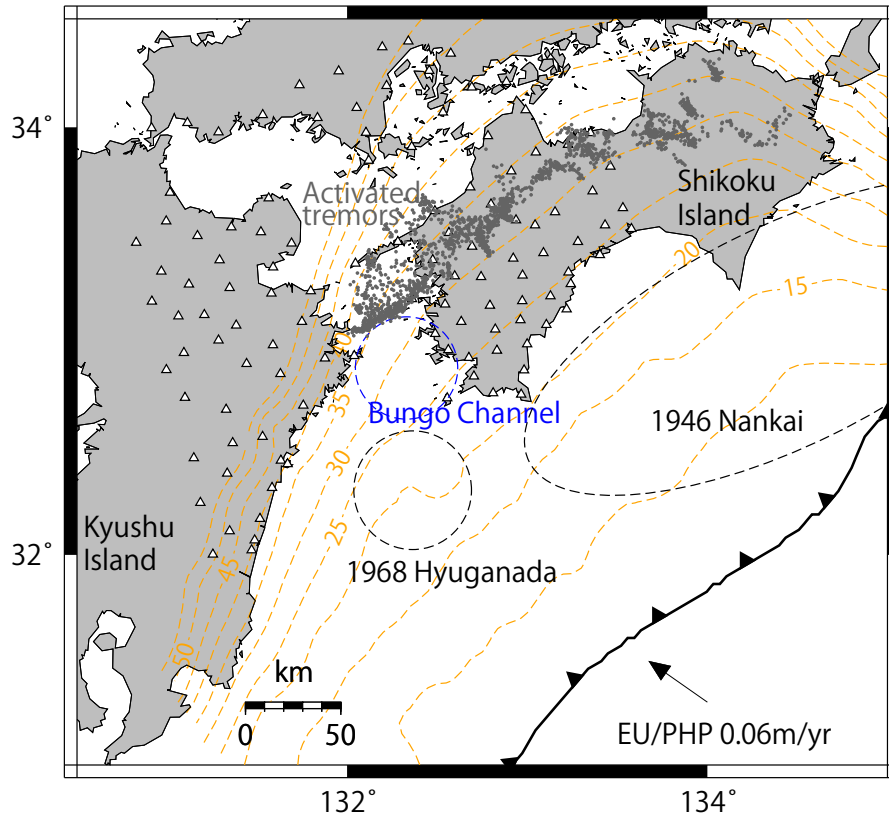


Figure 1. Tectonic setting for the target region. The blue dashed circle and the gray dots denote the location of the Bungo Channel and estimated hypocenters of tectonic tremors (Maeda & Obara, 2009; Obara, 2010; Kano et al., 2018) during the 2010 L-SSE. The ellipses with dashed lines indicate the approximate source areas of the 1946 Nankai and 1968 Hyuga-nada earthquakes. The orange dashed lines are the iso-depth contours drawn every five kilometers of the Nakanishi model as an example. The white triangles denote the locations of GEONET stations. The black arrow denotes the direction of the plate convergence rate between the Philippine Sea Plate and the Eurasian Plate.

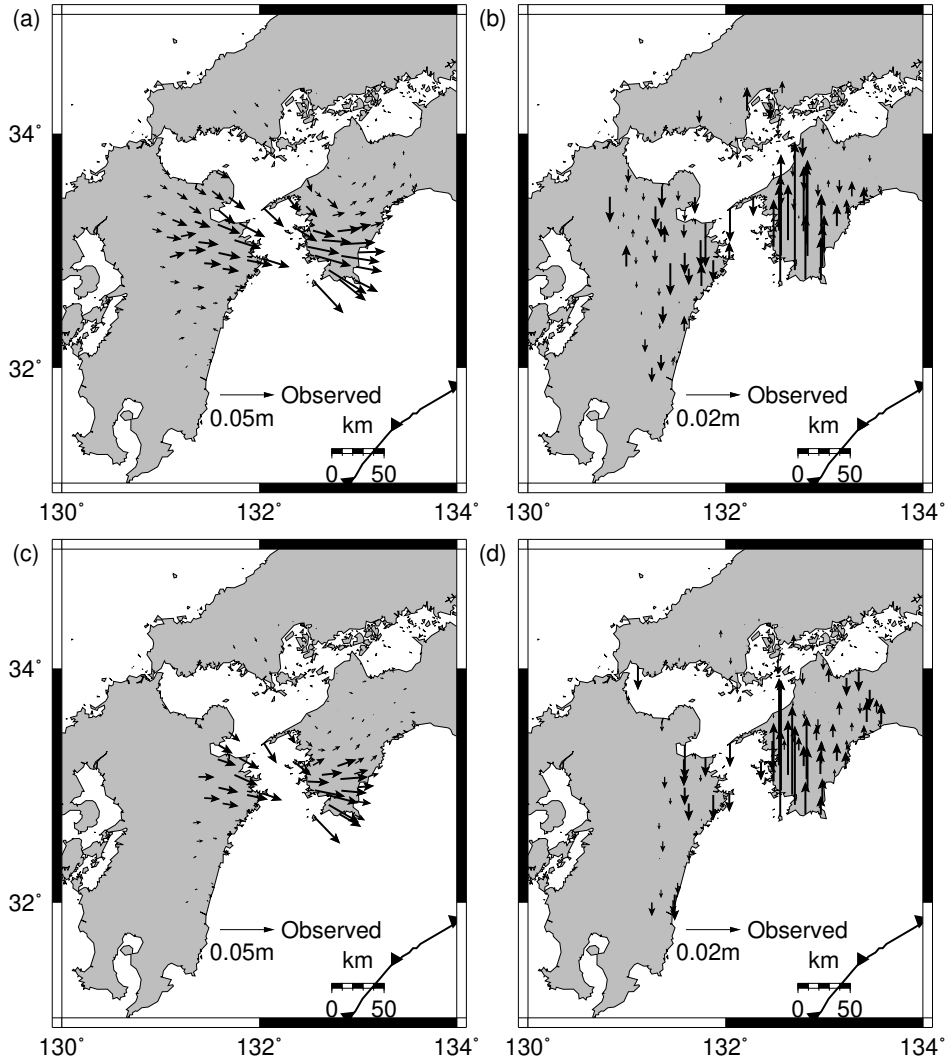


Figure 2. Surface displacement associated with the Bungo Channel L-SSE used in this study, derived from daily coordinates of GEONET (F3 solutions) by Yoshioka et al. (2015) and Seshimo and Yoshioka (2021). (a) Horizontal and (b) vertical displacements associated with the 2010 L-SSE. (c)(d) Those for the 2018 L-SSE.

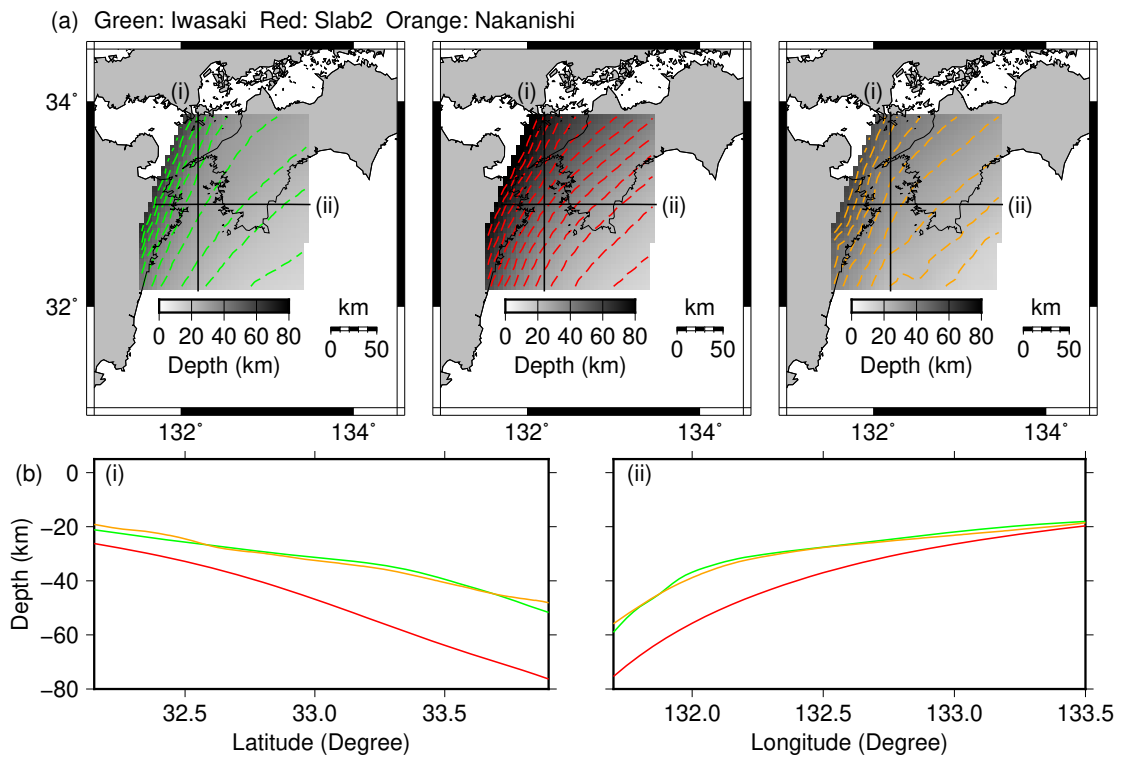


Figure 3. Comparison of three plate boundary geometry models, namely, the Iwasaki model, Slab2, and the Nakanishi model. (a) Plots of iso-depth contours for the three models. (b) Profiles on the lines denoted by (i) and (ii) in (a).

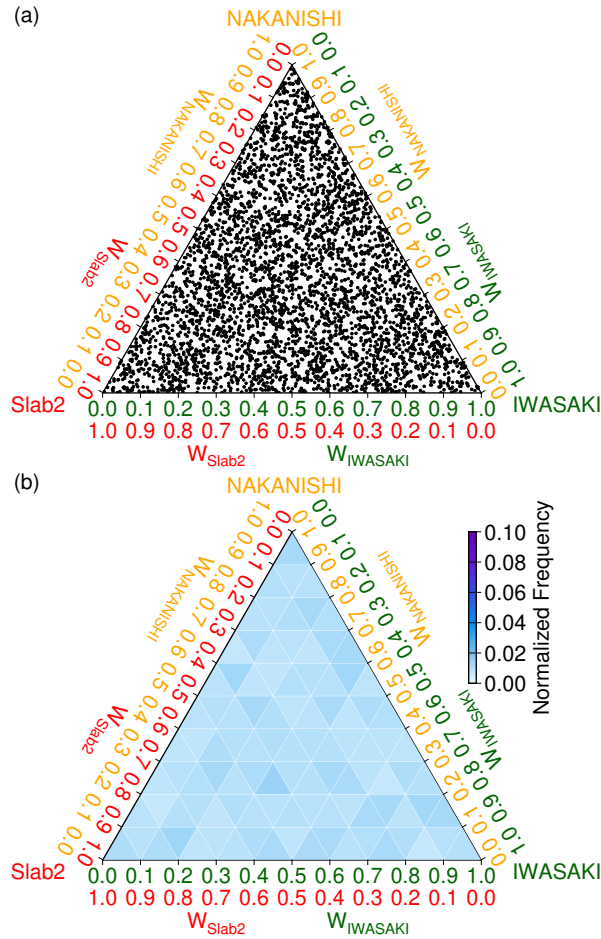


Figure 4. Ternary plots for the prior PDF for the plate boundary geometry model when the ensemble size N is taken to be 2,000. (a) Plot of 2,000 samples using dots (b) Color map for the normalized frequency in each small triangle.

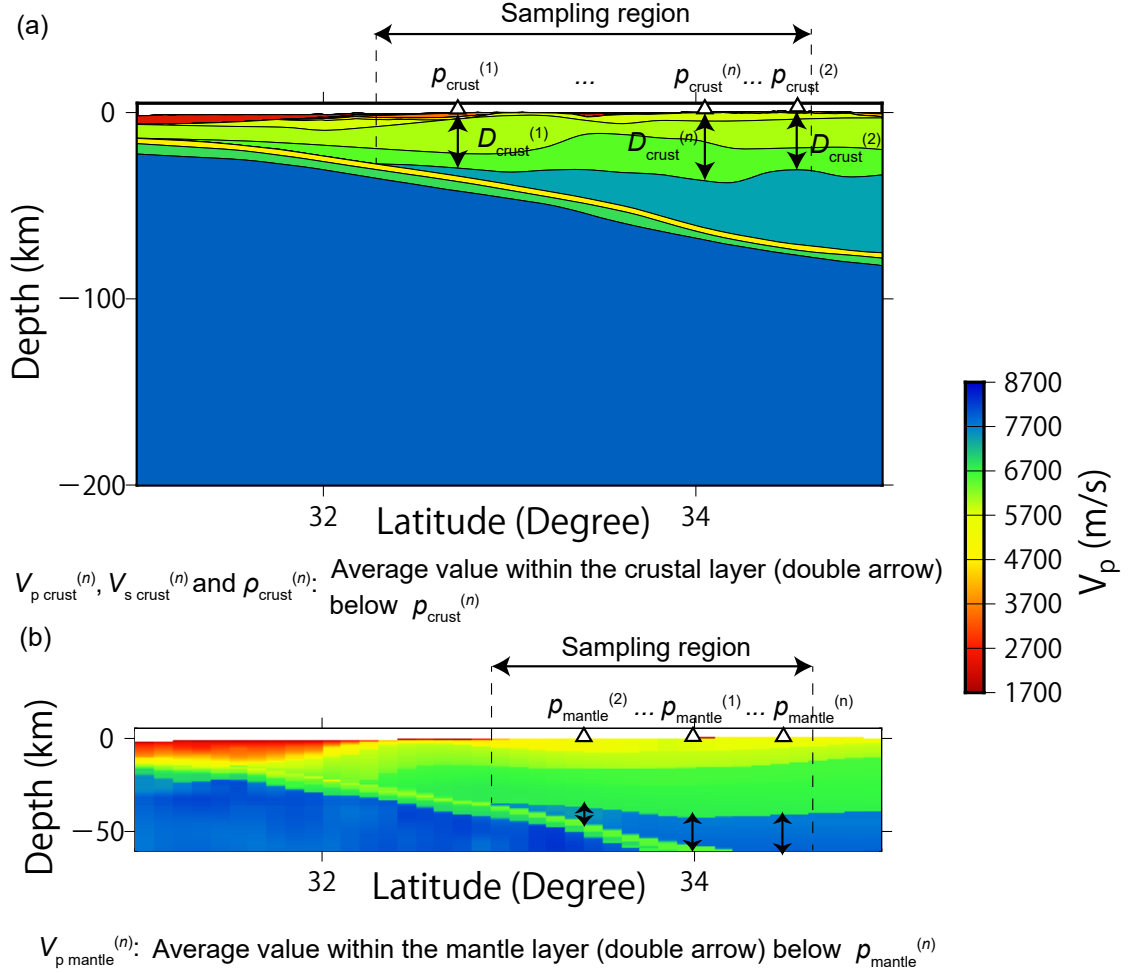


Figure 5. A two-dimensional schematic to explain the generation process of the random samples that consist of the ensemble to model the elastic structure with uncertainty. (a) Schematic of the samples of D_{crust} , $V_{p \text{ crust}}$, $V_{s \text{ crust}}$, and ρ_{crust} based on JIVSM (Koketsu et al., 2009, 2012). (b) For $V_{p \text{ mantle}}$ based on the 3D P-wave velocity model of Nakanishi et al. (2018) ($V_{s \text{ mantle}}$ and ρ_{mantle} are calculated based on an empirical relationship with $V_{p \text{ mantle}}$).

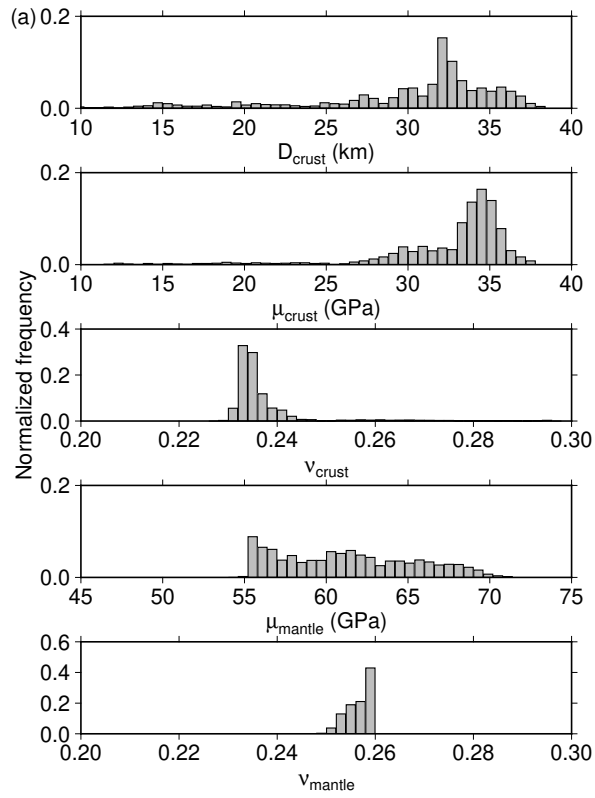


Figure 6. The histograms for the prior PDF of the elastic parameters when the ensemble size N is taken to be 2,000.

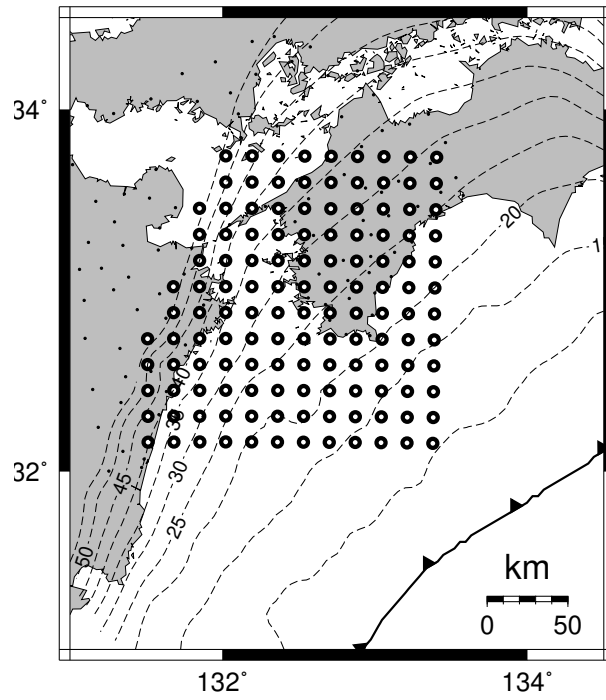


Figure 7. Configuration of slip parametrization. The black circles, dots, and dashed lines denote the central point of each small fault, the location of observation stations used in the 2010 estimation, and the iso-depth contour of the Nakanishi model as an example.

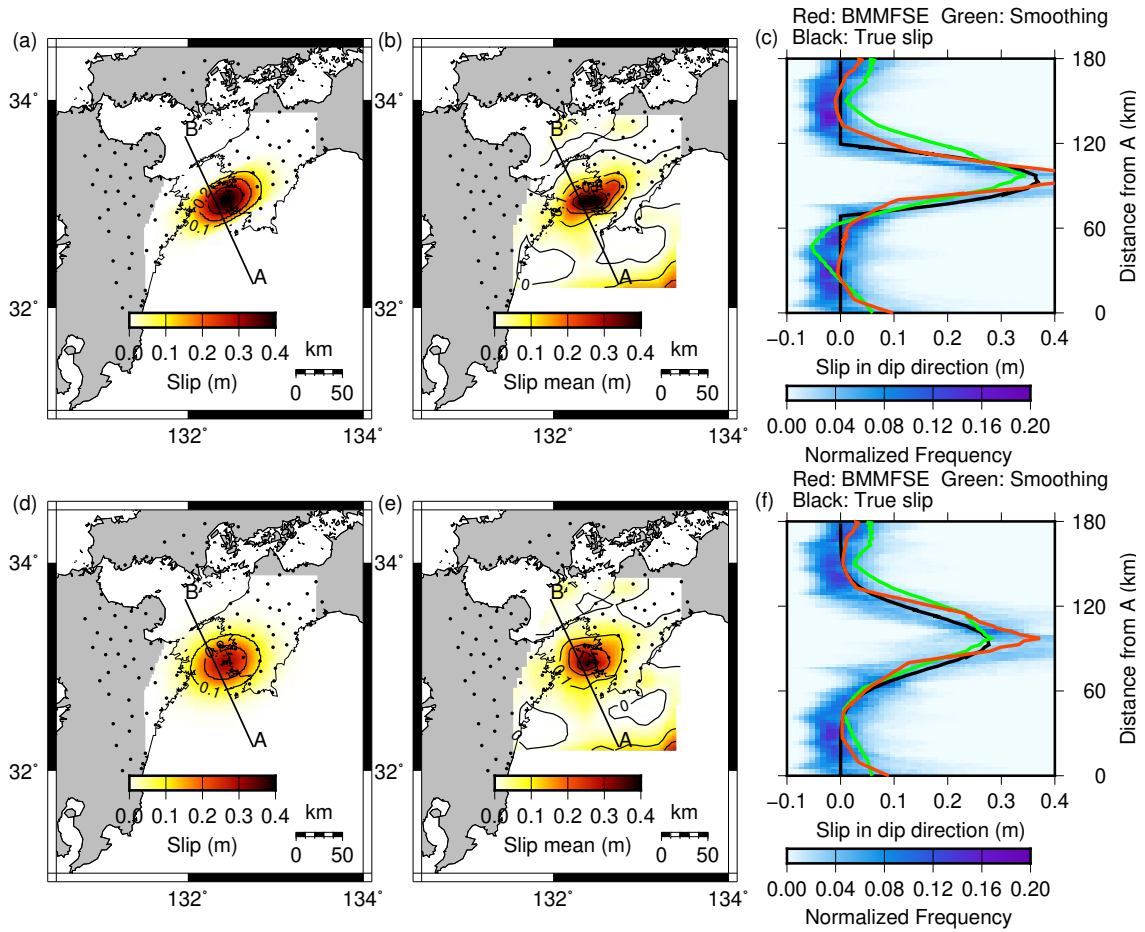


Figure 8. The estimation results for the numerical experiments. (a) True slip distribution of SM_{sharp} . (b) Mean model of the posterior PDF for the slip distribution estimated for SM_{sharp} using BMMFSE. (c) Comparison of the slip distribution estimated using BMMFSE, the smoothing model, and the true slip distribution on the A-B line profile is denoted in (a) and (b). (d)-(f) Same as (a)-(c) but for SM_{smooth} .

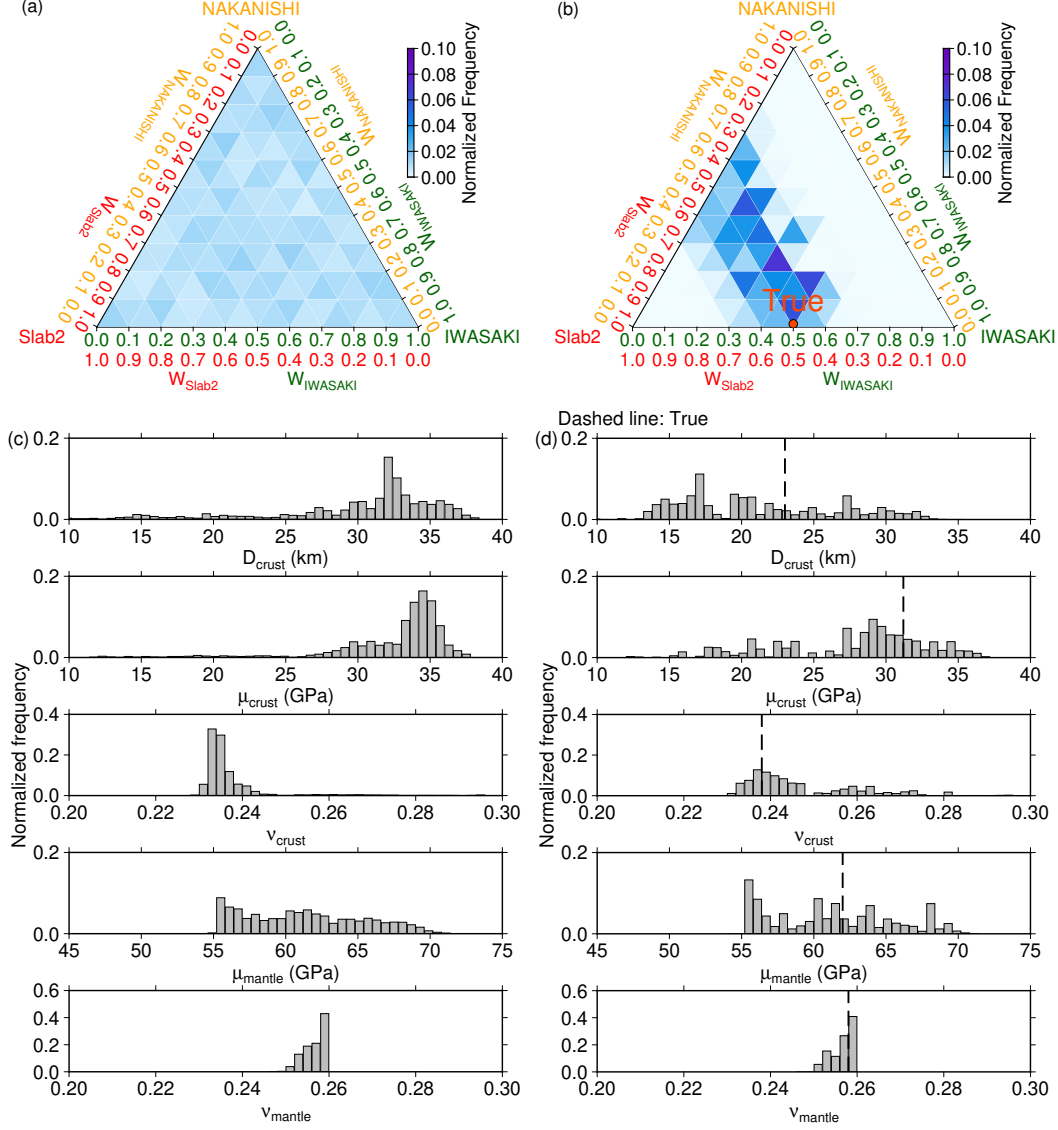


Figure 9. Comparison of the prior and posterior PDF of the underground structure in the numerical experiment for SM_{sharp} . Ternary plots for (a) the prior and (b) posterior PDFs of the plate boundary geometry model. Histograms illustrating (c) the prior and (d) posterior PDF of the elastic structure. (a) and (c) are identical to those in Figures 4 (b) and Figure 6.

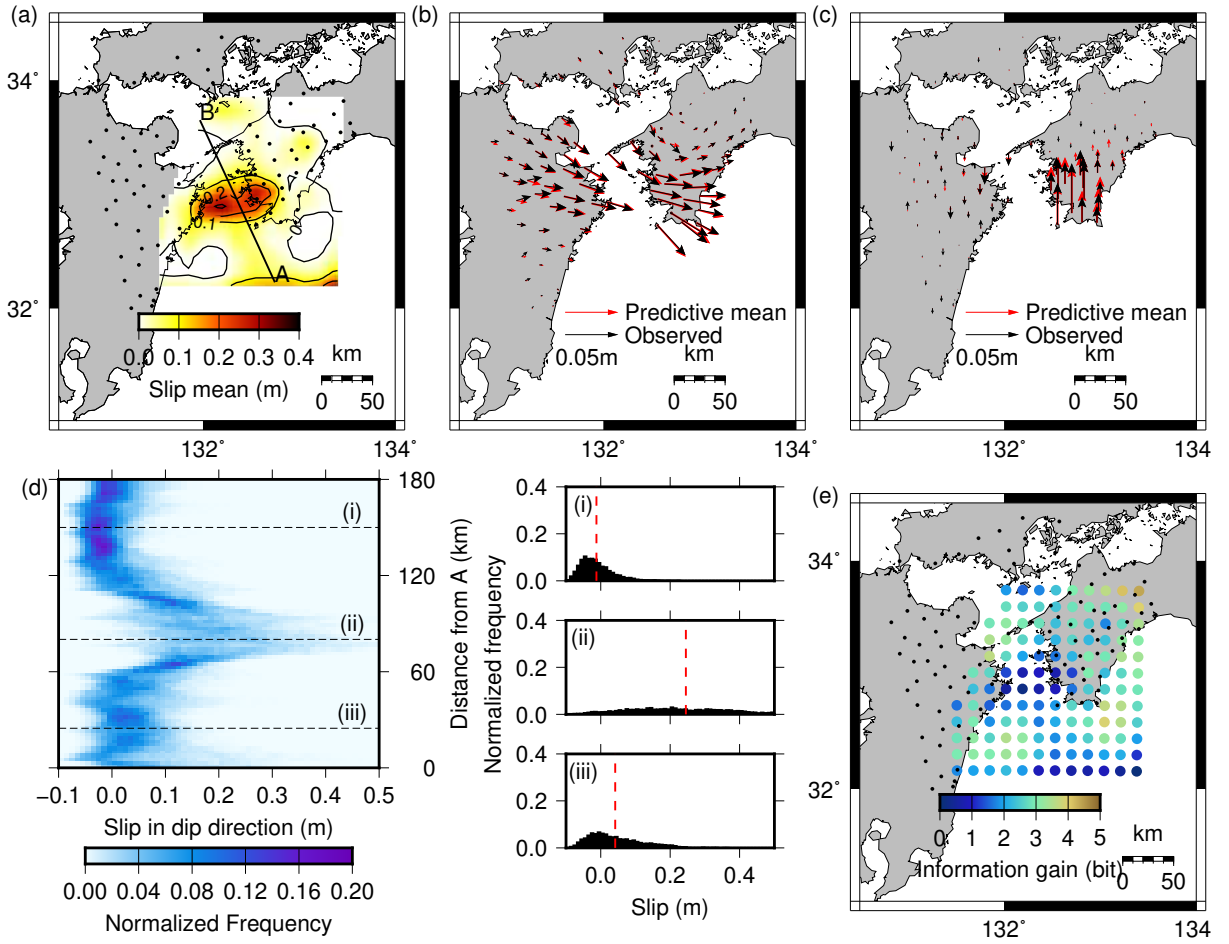


Figure 10. Estimation result of the slip distribution in the 2010 L-SSE obtained by using BMMFSE. (a) Mean model of posterior PDF for slip distribution. (b) Mean of the predictive PDF of and the observed horizontal displacement. (c) Vertical displacement (d) Color map of frequencies of amount of slip denoting the posterior PDF on the A-B line profile marked in (a) and the histograms in lines (i), (ii), and (iii) marked in the color map. The red dashed line denotes the mean values. (e) Information gain in Bayesian estimation for the 2010 L-SSE.

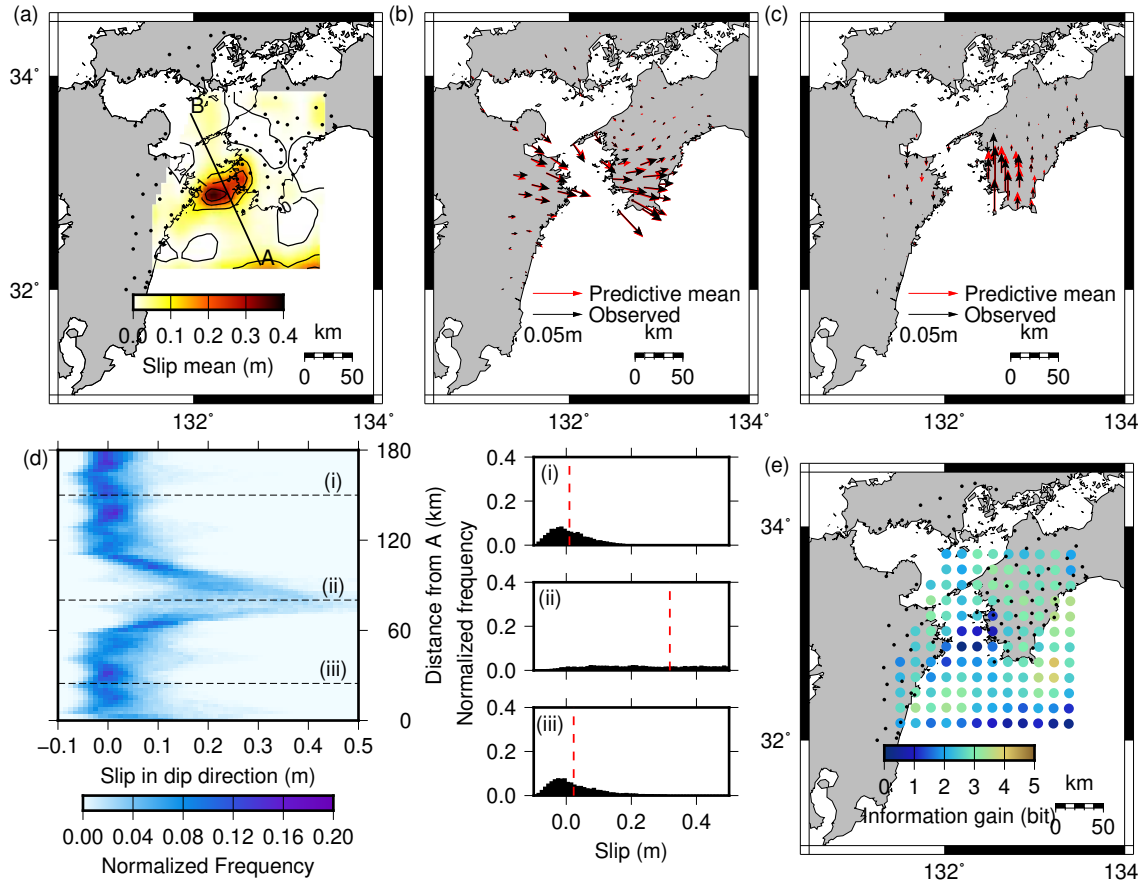


Figure 11. Estimation result of the slip distribution in the 2018 L-SSE obtained by using BMMFSE. (a) Mean model of posterior PDF for slip distribution. (b) Mean of the predictive PDF of and the observed horizontal displacement. (c) Vertical displacement (d) Color map of the frequencies of amount of slip denoting the posterior PDF on the A-B line profile marked in (a) and the histograms in lines (i), (ii), and (iii) marked in the color map. The red dashed line denotes the mean values. (e) Information gain in the Bayesian estimation for the 2018 L-SSE.

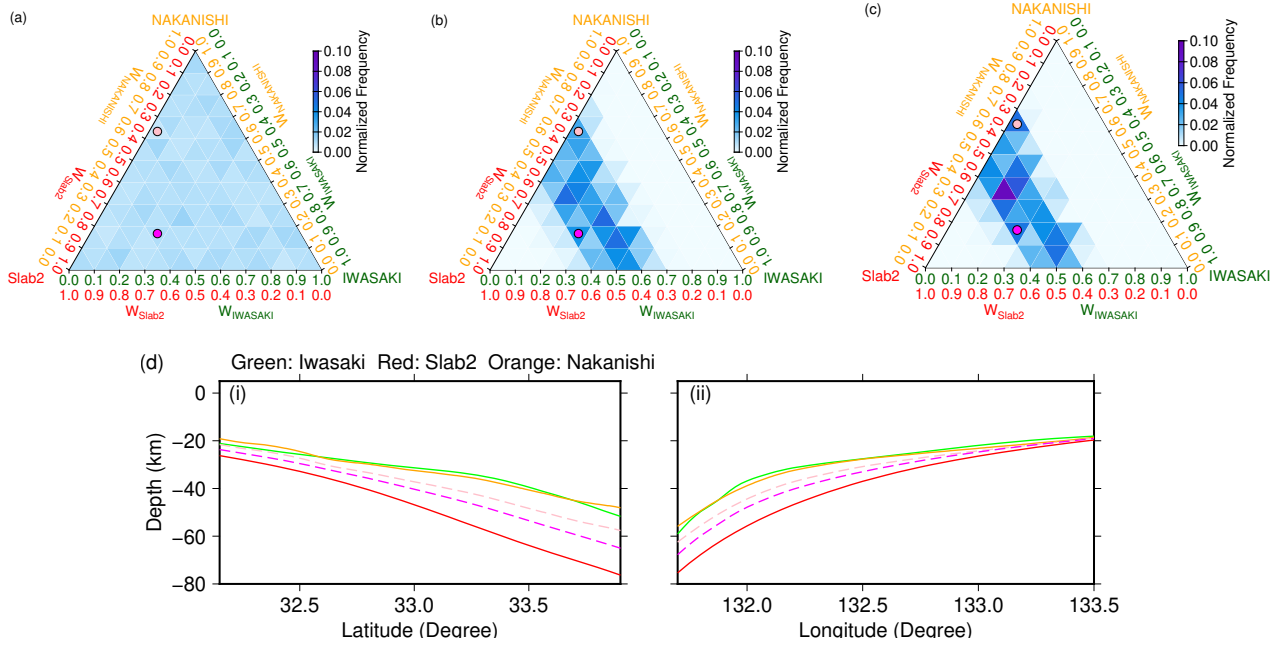


Figure 12. Comparison of ternary plots for the prior and posterior PDF of the plate boundary geometry model. (a) Prior PDF, which is identical to Figure 4 (b). (b) The posterior PDF obtained in the 2010 estimation. (c) For the 2018 estimation (d) Plate boundary geometries produced by the weights denoted by the locations marked by the pink and magenta circles in (a), (b), and (c), plotted in the same line profile shown in Figure 3.

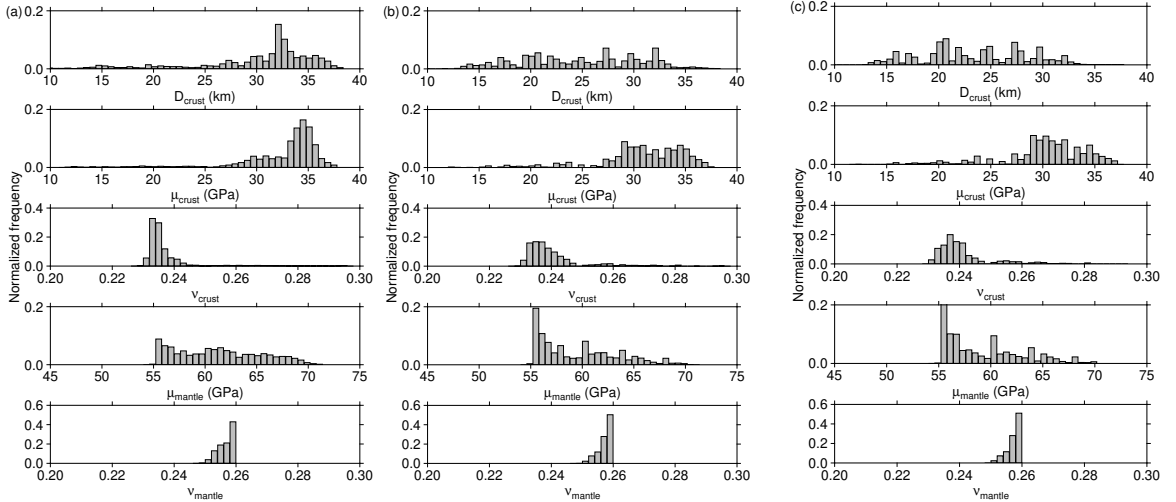


Figure 13. Comparison of the histogram plots for the prior and posterior PDF of the elastic parameters. (a) Prior PDF, which is identical to Figure 6. (b) The posterior PDF obtained in the 2010 estimation. (c) For 2018 L-SSE.

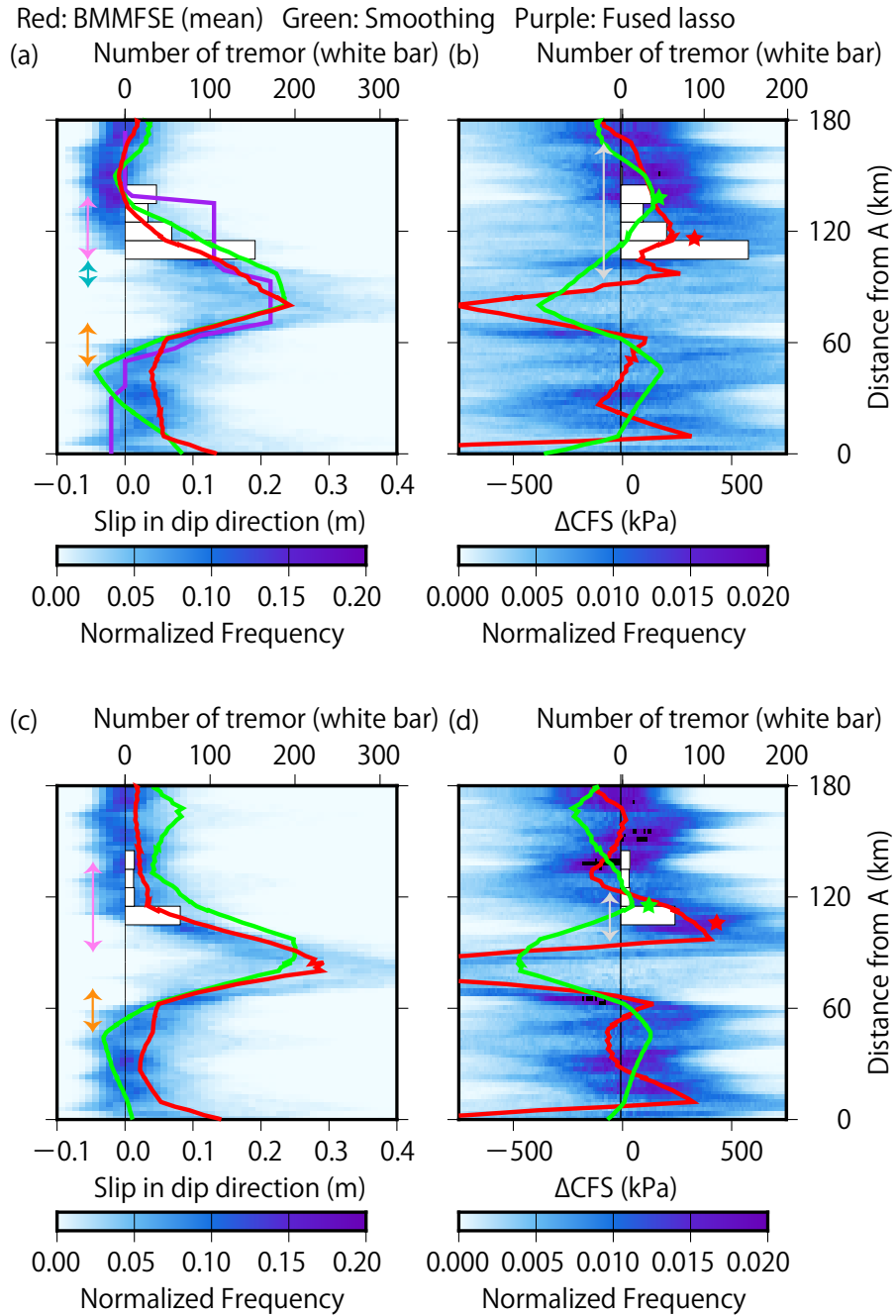


Figure 14. The correspondence between estimated slip distribution, Δ CFS and the tremor distribution on the A-B line profile. (a) Comparison of slip distribution models for 2010 L-SSE. The color map denotes the frequency of the amount of slip for the posterior PDF. The red, green, and purple lines denote the slip distribution of the mean of the BMMFSE, smoothing, and fused lasso models, respectively. (b) Comparison of the Δ CFS distributions for 2010 L-SSE. The color map denotes the frequencies of the Δ CFS values for the posterior PDF. The red and green lines denote the distribution of the mean of Δ CFS calculated based on the posterior PDF of the slip distribution estimated by BMMFSE and the Δ CFS distribution calculated based on the slip distribution of the smoothing model, respectively. The location of the peak of the positive value of the mean Δ CFS in the down-dip side of the channel for BMMFSE and the smoothing model are denoted by red and green stars, respectively. In all the figures, the white bars denote the number of tremors during the L-SSE period in the area within 5 km from the line in the direction perpendicular to it. (c)(d) Those for the 2018 L-SSE.

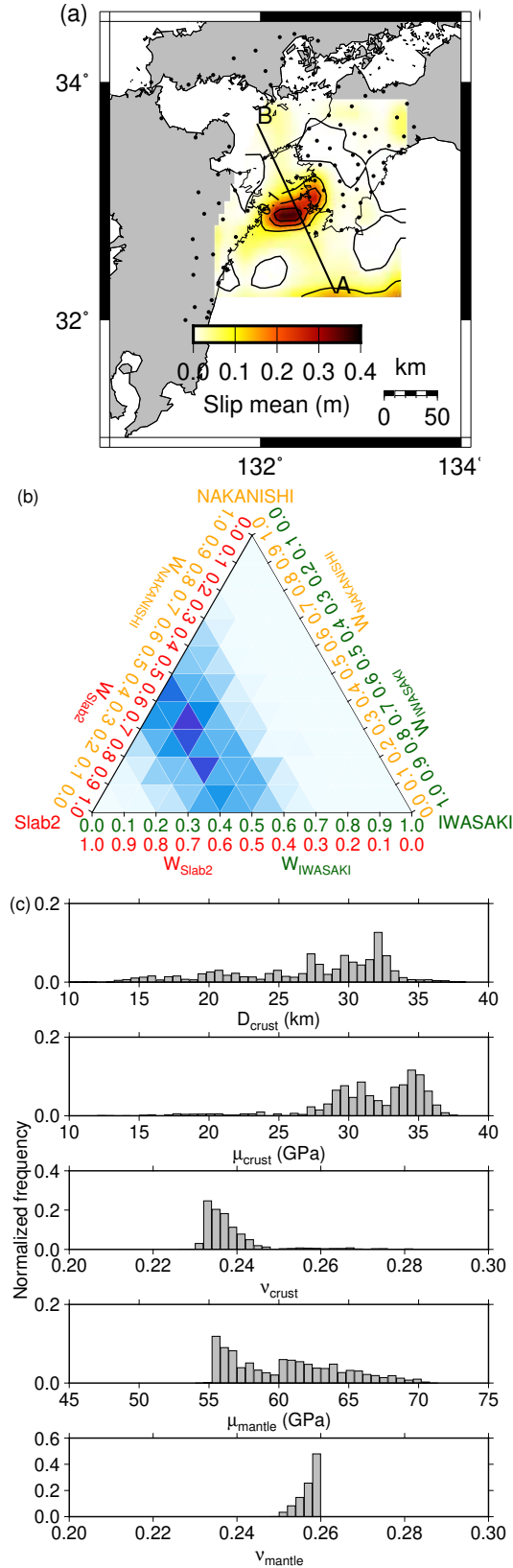


Figure 15. The estimation results for the 2018 L-SSE using the original prior PDF instead of the PDF for the underground structure updated through estimation for the 2010 one. (a) The mean slip distribution, the posterior PDF for (b) the plate boundary geometry and (c) the elastic structure.

919 **Appendix A Approximation of $P(\varphi)$ based on the particle approx-**
 920 **imation with importance weights**

921 The formulation described in Section 3.1 is based on a simple particle approxi-
 922 mation of $P(\varphi)$ as

$$P(\varphi) \simeq \frac{1}{N} \sum_{n=1}^N \delta(\varphi - \varphi^{(n)}). \quad (\text{A1})$$

923 The evaluation of the posterior PDF of \mathbf{m} and φ is based on the particle approxima-
 924 tion with importance weights, such as

$$P(\varphi) \simeq \frac{1}{N} \sum_{n=1}^N g^{(n)} \delta(\varphi - \varphi^{(n)}), \quad (\text{A2})$$

925 is also readily applicable as follows:

$$P(\mathbf{m}|\mathbf{d}) \simeq \kappa \frac{1}{N} \sum_{n=1}^N g^{(n)} P(\mathbf{d}|\mathbf{m}, \varphi^{(n)}) P(\mathbf{m}|\varphi^{(n)}) \quad (\text{A3})$$

$$P(\varphi|\mathbf{d}) \simeq \frac{1}{N} \sum_{n=1}^N g^{(n)} w^{(n)} \delta(\varphi - \varphi^{(n)}). \quad (\text{A4})$$

926 **Appendix B The definition of the cosine tapered-uniform distribu-**
 927 **tion**

928 The PDF is for a cosine-tapered uniform distribution $U_{\cos}(a', a, b, b')$, and is
 929 defined as

$$P(x) = \kappa f(x), \quad (\text{B1})$$

930 where

$$f(x) = \begin{cases} \frac{1}{2} \left(-\cos \left(\frac{x - a'}{a - a'} \pi \right) + 1 \right) & (a' \leq x < a) \\ 1 & (a \leq x \leq b) \\ \frac{1}{2} \left(\cos \left(\frac{x - b}{b' - b} \pi \right) + 1 \right) & (b < x \leq b') \\ 0 & (\textit{else}) \end{cases} \quad (\text{B2})$$

931 and κ is the normalizing factor.

932 **Appendix C The definition and calculation of the posterior predic-**
 933 **tive PDF**

934 The definition of the posterior predictive PDF for a certain physical quantity \mathbf{x}
 935 (using a vector notation to maintain generality), for example, surface displacement,
 936 seismic moment release, and ΔCFS as presented in the main text, based on the esti-
 937 mated Bayesian model is written as:

$$P(\mathbf{x}|\mathbf{D}) = \int \int P(\mathbf{x}|\mathbf{m}, \varphi) P(\mathbf{m}, \varphi|\mathbf{D}) d\mathbf{m} d\varphi, \quad (\text{C1})$$

938 where $P(\mathbf{m}, \varphi|\mathbf{D})$ is the joint posterior PDF of the model and the underground
 939 structure parameters obtained using the data $\mathbf{d} = \mathbf{D}$. After performing the REMC

940 sampling, the double integration on the right-hand side of this equation is approxi-
 941 mately evaluated as:

$$P(\mathbf{x}|\mathbf{D}) \simeq \frac{1}{M} \sum_{m=1}^M \int P(\mathbf{x}|\mathbf{m}^{(m)}, \boldsymbol{\varphi}) \frac{P(\mathbf{D}|\mathbf{m}^{(m)}, \boldsymbol{\varphi})P(\boldsymbol{\varphi})}{\frac{1}{N} \sum_{n=1}^N P(\mathbf{D}|\mathbf{m}^{(m)}, \boldsymbol{\varphi}^{(n)})} d\boldsymbol{\varphi} \quad (\text{C2})$$

$$\simeq \frac{1}{NM} \sum_{n=1}^N \sum_{m=1}^M P(\mathbf{x}|\mathbf{m}^{(m)}, \boldsymbol{\varphi}^{(n)}) \frac{P(\mathbf{D}|\mathbf{m}^{(m)}, \boldsymbol{\varphi}^{(n)})}{\frac{1}{N} \sum_{n'=1}^N P(\mathbf{D}|\mathbf{m}^{(m)}, \boldsymbol{\varphi}^{(n')})}, \quad (\text{C3})$$

942 where the value of $P(\mathbf{D}|\mathbf{m}^{(m)}, \boldsymbol{\varphi}^{(n)})$ for each sample with the indices m and n is al-
 943 ready available (see Equation 5 and the explanation therein).

Acknowledgments

We appreciate the discussions on the plate boundary geometry model by Dr Ayako Nakanishi and Dr Yojiro Yamamoto. This research was supported by JSPS KAKENHI Grant Number JP16H06472 and JP19H04631 in Scientific Research on Innovative Areas “Science of Slow Earthquakes”. The plate models by Iwasaki et al. (2015) were constructed from topography and bathymetry data by Geospatial Information Authority of Japan (250-m digital map), Japan Oceanographic Data Center (500m mesh bathymetry data, J-EGG500, http://www.jodc.go.jp/jodcweb/JDOSS/infoJEGG_j.html) and Geographic Information Network of Alaska, University of Alaska (Lindquist et al., 2004). This research was conducted using the Fujitsu PRIMERGY CX400M1/CX2550M5 (Oakbridge-CX) in the Information Technology Center, The University of Tokyo. Computational resources of the Earth Simulator 4 provided by JAMSTEC was also used.

References

- Agata, R., Ichimura, T., Hori, T., Hirahara, K., Hashimoto, C., & Hori, M. (2018). An adjoint-based simultaneous estimation method of the asthenosphere’s viscosity and afterslip using a fast and scalable finite-element adjoint solver. *Geophysical Journal International*, *213*(1), 461–474. Retrieved from <http://dx.doi.org/10.1093/gji/ggx561> doi: 10.1093/gji/ggx561
- Agata, R., Kasahara, A., & Yagi, Y. (2021). A bayesian inference framework for fault slip distributions based on ensemble modelling of the uncertainty of underground structure: with a focus on uncertain fault dip. *Geophysical Journal International*, *225*(2), 1392–1411.
- Amey, R., Hooper, A., & Morishita, Y. (2019). Going to Any Lengths: Solving for Fault Size and Fractal Slip for the 2016, M w 6.2 Central Tottori Earthquake, Japan, Using a Transdimensional Inversion Scheme. *Journal of Geophysical Research: Solid Earth*, *124*(4), 4001–4016.
- Amey, R., Hooper, A., & Walters, R. (2018). A Bayesian method for incorporating self-similarity into earthquake slip inversions. *Journal of Geophysical Research: Solid Earth*, *123*(7), 6052–6071.
- Baba, T., Tanioka, Y., Cummins, P. R., & Uhira, K. (2002). The slip distribution of the 1946 Nankai earthquake estimated from tsunami inversion using a new plate model. *Physics of the Earth and Planetary Interiors*, *132*(1-3), 59–73.
- Bartlow, N. M., Miyazaki, S., Bradley, A. M., & Segall, P. (2011). Space-time correlation of slip and tremor during the 2009 Cascadia slow slip event. *Geophysical Research Letters*, *38*(18).
- Bartlow, N. M., Wallace, L. M., Beavan, R. J., Bannister, S., & Segall, P. (2014). Time-dependent modeling of slow slip events and associated seismicity and tremor at the Hikurangi subduction zone, New Zealand. *Journal of Geophysical Research: Solid Earth*, *119*(1), 734–753.
- Brocher, T. M. (2005). Empirical relations between elastic wavespeeds and density in the Earth’s crust. *Bulletin of the seismological Society of America*, *95*(6), 2081–2092.
- Comninou, M., & Dundurs, J. (1975). The angular dislocation in a half space. *Journal of Elasticity*, *5*(3-4), 203–216.
- Dettmer, J., Benavente, R., Cummins, P. R., & Sambridge, M. (2014). Transdimensional finite-fault inversion. *Geophysical Journal International*, *199*(2), 735–751.
- Duputel, Z., Agram, P. S., Simons, M., Minson, S. E., & Beck, J. L. (2014). Accounting for prediction uncertainty when inferring subsurface fault slip. *Geophysical Journal International*, *197*(1), 464–482.
- Frank, W. B., Shapiro, N. M., Husker, A. L., Kostoglodov, V., Bhat, H. S., & Campillo, M. (2015). Along-fault pore-pressure evolution during a slow-slip

- 997 event in Guerrero, Mexico. *Earth and Planetary Science Letters*, *413*, 135–
 998 143.
- 999 Fukahata, Y., & Matsu'ura, M. (2006, jul). Quasi-static internal deformation due
 1000 to a dislocation source in a multilayered elastic/viscoelastic half-space and
 1001 an equivalence theorem. *Geophysical Journal International*, *166*(1), 418–
 1002 434. Retrieved from [http://gji.oxfordjournals.org/cgi/doi/10.1111/
 1003 j.1365-246X.2006.02921.x](http://gji.oxfordjournals.org/cgi/doi/10.1111/j.1365-246X.2006.02921.x) doi: 10.1111/j.1365-246X.2006.02921.x
- 1004 Fukahata, Y., & Wright, T. J. (2008). A non-linear geodetic data inversion using
 1005 ABIC for slip distribution on a fault with an unknown dip angle. *Geophysical
 1006 Journal International*, *173*(2), 353–364.
- 1007 Fukuda, J., & Johnson, K. M. (2008). A fully bayesian inversion for spatial dis-
 1008 tribution of fault slip with objective smoothing. *Bulletin of the Seismological
 1009 Society of America*, *98*(3), 1128–1146.
- 1010 Fukuda, J., & Johnson, K. M. (2010). Mixed linear–non–linear inversion of crustal
 1011 deformation data: Bayesian inference of model, weighting and regularization
 1012 parameters. *Geophysical Journal International*, *181*(3), 1441–1458.
- 1013 Geyer, C. J. (1991). Markov chain Monte Carlo maximum likelihood.
- 1014 Gordon, N. J., Salmond, D. J., & Smith, A. F. (1993). Novel approach to
 1015 nonlinear/non-Gaussian Bayesian state estimation. In *Iee proceedings f (radar
 1016 and signal processing)* (Vol. 140, pp. 107–113).
- 1017 Hayes, G. P., Moore, G. L., Portner, D. E., Hearne, M., Flamme, H., Furtney, M.,
 1018 & Smoczyk, G. M. (2018). Slab2, a comprehensive subduction zone geometry
 1019 model. *Science*, *362*(6410), 58–61.
- 1020 Heki, K., & Miyazaki, S. (2001). Plate convergence and long-term crustal deforma-
 1021 tion in central japan. *Geophysical Research Letters*, *28*(12), 2313–2316.
- 1022 Hirose, H., Asano, Y., Obara, K., Kimura, T., Matsuzawa, T., Tanaka, S., & Maeda,
 1023 T. (2010). Slow earthquakes linked along dip in the Nankai subduction zone.
 1024 *Science*, *330*(6010), 1502–1502.
- 1025 Hirose, H., & Kimura, T. (2020). Slip distributions of short-Term slow slip events
 1026 in Shikoku, southwest Japan, from 2001 to 2019 based on tilt change measure-
 1027 ments. *Journal of Geophysical Research: Solid Earth*, *125*(6), e2020JB019601.
- 1028 Hirose, H., Matsuzawa, T., Kimura, T., & Kimura, H. (2014). The Boso slow slip
 1029 events in 2007 and 2011 as a driving process for the accompanying earthquake
 1030 swarm. *Geophysical Research Letters*, *41*(8), 2778–2785.
- 1031 Houston, H. (2015). Low friction and fault weakening revealed by rising sensitivity
 1032 of tremor to tidal stress. *Nature Geoscience*, *8*(5), 409–415.
- 1033 Iwasaki, T., Sato, H., Ishiyama, T., Shinohara, M., & Hashima, A. (2015). Fun-
 1034 damental structure model of island arcs and subducted plates in and around
 1035 japan. In *Agu fall meeting abstracts* (Vol. 2015, pp. T31B–2878).
- 1036 Kano, M., Aso, N., Matsuzawa, T., Ide, S., Annoura, S., Arai, R., . . . others (2018).
 1037 Development of a slow earthquake database. *Seismological Research Letters*,
 1038 *89*(4), 1566–1575.
- 1039 Kano, M., Kato, A., & Obara, K. (2019). Episodic tremor and slip silently invades
 1040 strongly locked megathrust in the Nankai Trough. *Scientific reports*, *9*(1), 1–
 1041 8.
- 1042 Kass, R. E., & Raftery, A. E. (1995). Bayes factors. *Journal of the american statis-
 1043 tical association*, *90*(430), 773–795.
- 1044 Kitagawa, G. (1993). A Monte Carlo filtering and smoothing method for non-
 1045 Gaussian nonlinear state spacemodels. *Technical report, Institute of Statistical
 1046 Mathematics Research Memorandum*(462).
- 1047 Kitagawa, G. (1996). Monte Carlo filter and smoother for non-Gaussian nonlinear
 1048 state space models. *Journal of computational and graphical statistics*, *5*(1),
 1049 1–25.
- 1050 Koketsu, K., Miyake, H., & Suzuki, H. (2012). Japan integrated velocity structure
 1051 model version 1. *Proceedings of the 15th World Conference on Earthquake*

- 1052 *Engineering*(1773).
- 1053 Koketsu, K., Miyake, H., Tanaka, Y., et al. (2009). A proposal for a standard pro-
 1054 cedure of modeling 3-D velocity structures and its application to the Tokyo
 1055 metropolitan area, Japan. *Tectonophysics*, 472(1-4), 290–300.
- 1056 Kostoglodov, V., Husker, A., Shapiro, N. M., Payero, J. S., Campillo, M., Cotte, N.,
 1057 & Clayton, R. (2010). The 2006 slow slip event and nonvolcanic tremor in the
 1058 Mexican subduction zone. *Geophysical Research Letters*, 37(24).
- 1059 Li, S., & Barnhart, W. D. (2020). Impacts of topographic relief and crustal hetero-
 1060 geneity on coseismic deformation and inversions for fault geometry and slip: A
 1061 case study of the 2015 Gorkha earthquake in the central Himalayan arc. *Geo-
 1062 chemistry, Geophysics, Geosystems*, 21(12), e2020GC009413.
- 1063 Lindquist, K. G., Engle, K., Stahlke, D., & Price, E. (2004). Global topography
 1064 and bathymetry grid improves research efforts. *Eos, Transactions American
 1065 Geophysical Union*, 85(19), 186–186.
- 1066 Lindsey, E., & Fialko, Y. (2013). Geodetic slip rates in the southern San Andreas
 1067 Fault system: Effects of elastic heterogeneity and fault geometry. *Journal of
 1068 Geophysical Research: Solid Earth*, 118(2), 689–697.
- 1069 Maeda, T., & Obara, K. (2009). Spatiotemporal distribution of seismic energy ra-
 1070 diation from low-frequency tremor in western Shikoku, Japan. *Journal of Geo-
 1071 physical Research: Solid Earth*, 114(B10).
- 1072 Metropolis, N., Rosenbluth, A. W., Rosenbluth, M. N., Teller, A. H., & Teller, E.
 1073 (1953). Equation of state calculations by fast computing machines. *The journal
 1074 of chemical physics*, 21(6), 1087–1092.
- 1075 Minson, S., Murray, J. R., Langbein, J. O., & Gomberg, J. S. (2014). Real-time
 1076 inversions for finite fault slip models and rupture geometry based on high-rate
 1077 GPS data. *Journal of Geophysical Research: Solid Earth*, 119(4), 3201–3231.
- 1078 Minson, S., Simons, M., & Beck, J. (2013). Bayesian inversion for finite fault earth-
 1079 quake source models I—Theory and algorithm. *Geophysical Journal Interna-
 1080 tional*, 194(3), 1701–1726.
- 1081 Miyazaki, S., & Hatanaka, Y. (1998). The outlines of the GEONET (in Japanese).
 1082 *Meteorol. Res. Note*, 192, 105–131.
- 1083 Nakanishi, A., Takahashi, N., Yamamoto, Y., Takahashi, T., Citak, S. O., Naka-
 1084 mura, T., . . . Kaneda, Y. (2018). Three-dimensional plate geometry and P-
 1085 wave velocity models of the subduction zone in SW Japan: Implications for
 1086 seismogenesis. *Geology and Tectonics of Subduction Zones: A Tribute to Gaku
 1087 Kimura*, 534, 69.
- 1088 Nakata, R., Hino, H., Kuwatani, T., Yoshioka, S., Okada, M., & Hori, T. (2017).
 1089 Discontinuous boundaries of slow slip events beneath the Bungo Channel,
 1090 southwest Japan. *Scientific reports*, 7(1), 6129.
- 1091 Nakata, R., Kuwatani, T., Okada, M., & Hori, T. (2016). Geodetic inversion for
 1092 spatial distribution of slip under smoothness, discontinuity, and sparsity con-
 1093 straints. *Earth, Planets and Space*, 68(1), 1–10.
- 1094 Obara, K. (2010). Phenomenology of deep slow earthquake family in southwest
 1095 Japan: Spatiotemporal characteristics and segmentation. *Journal of Geophys-
 1096 ical Research: Solid Earth*, 115(B8).
- 1097 Obara, K., Hirose, H., Yamamizu, F., & Kasahara, K. (2004). Episodic slow slip
 1098 events accompanied by non-volcanic tremors in southwest Japan subduction
 1099 zone. *Geophysical Research Letters*, 31(23).
- 1100 Obara, K., & Kato, A. (2016). Connecting slow earthquakes to huge earthquakes.
 1101 *Science*, 353(6296), 253–257.
- 1102 Ozawa, S., Kawabata, R., Kokado, K., & Yarai, H. (2020). Long-term slow slip
 1103 events along the Nankai trough delayed by the 2016 Kumamoto earthquake,
 1104 Japan. *Earth, Planets and Space*, 72, 1–9.
- 1105 Raftery, A. E., Madigan, D., & Hoeting, J. A. (1997). Bayesian model averaging
 1106 for linear regression models. *Journal of the American Statistical Association*,

- 1107 92(437), 179–191.
- 1108 Rogers, G., & Dragert, H. (2003). Episodic tremor and slip on the Cascadia subduc-
1109 tion zone: The chatter of silent slip. *Science*, 300(5627), 1942–1943.
- 1110 Seshimo, Y., & Yoshioka, S. (2021). Spatiotemporal slip distributions of the 2018-
1111 2019 Bungo Channel long-term slow slip event. *Japan Geoscience Union Meet-
1112 ing 2021*.
- 1113 Shimizu, K., Yagi, Y., Okuwaki, R., & Fukahata, Y. (2021). Construction of fault
1114 geometry by finite-fault inversion of teleseismic data. *Geophysical Journal In-
1115 ternational*, 224(2), 1003–1014.
- 1116 Swendsen, R. H., & Wang, J.-S. (1986). Replica Monte Carlo simulation of spin-
1117 glasses. *Physical review letters*, 57(21), 2607.
- 1118 Takagi, R., Uchida, N., & Obara, K. (2019). Along-strike variation and migration
1119 of long-term slow slip events in the western Nankai subduction zone, Japan.
1120 *Journal of Geophysical Research: Solid Earth*, 124(4), 3853–3880.
- 1121 Tibshirani, R., Saunders, M., Rosset, S., Zhu, J., & Knight, K. (2005). Sparsity and
1122 smoothness via the fused lasso. *Journal of the Royal Statistical Society: Series
1123 B (Statistical Methodology)*, 67(1), 91–108.
- 1124 Villafuerte, C., & Cruz-Atienza, V. M. (2017). Insights into the causal relationship
1125 between slow slip and tectonic tremor in Guerrero, Mexico. *Journal of Geo-
1126 physical Research: Solid Earth*, 122(8), 6642–6656.
- 1127 Wang, R., Martín, F. L., & Roth, F. (2003). Computation of deformation in-
1128 duced by earthquakes in a multi-layered elastic crust-FORTRAN programs
1129 EDGRN/EDCMP. *Computers & Geosciences*, 29(2), 195–207.
- 1130 Watanabe, S. (2013). A widely applicable bayesian information criterion. *Journal of
1131 Machine Learning Research*, 14(Mar), 867–897.
- 1132 Yabuki, T., & Matsu'ura, M. (1992). Geodetic data inversion using a Bayesian in-
1133 formation criterion for spatial distribution of fault slip. *Geophysical Journal
1134 International*, 109(2), 363–375. Retrieved from [http://gji.oxfordjournals
1135 .org/cgi/doi/10.1111/j.1365-246X.1992.tb00102.x](http://gji.oxfordjournals.org/cgi/doi/10.1111/j.1365-246X.1992.tb00102.x) doi: 10.1111/
1136 j.1365-246X.1992.tb00102.x
- 1137 Yagi, Y., & Fukahata, Y. (2008). Importance of covariance components in inver-
1138 sion analyses of densely sampled observed data: an application to waveform
1139 data inversion for seismic source processes. *Geophysical Journal International*,
1140 175(1), 215–221.
- 1141 Yagi, Y., & Fukahata, Y. (2011). Introduction of uncertainty of green's function into
1142 waveform inversion for seismic source processes. *Geophysical Journal Interna-
1143 tional*, 186(2), 711–720.
- 1144 Yamamoto, Y., Obana, K., Takahashi, T., Nakanishi, A., Kodaira, S., & Kaneda,
1145 Y. (2013). Imaging of the subducted Kyushu-Palau Ridge in the Hyuga-nada
1146 region, western Nankai Trough subduction zone. *Tectonophysics*, 589, 90–102.
- 1147 Yoshioka, S., Matsuoka, Y., & Ide, S. (2015). Spatiotemporal slip distributions of
1148 three long-term slow slip events beneath the Bungo Channel, southwest Japan,
1149 inferred from inversion analyses of GPS data. *Geophysical Journal Interna-
1150 tional*, 201(3), 1437–1455.

1 **Supporting Information for “Bayesian multi-model**
2 **estimation for fault slip distribution: the effect of**
3 **prior constraints in the estimation for slow slip events**
4 **beneath the Bungo Channel, southwest Japan”**

R. Agata¹, R. Nakata², A. Kasahara³, Y. Yagi⁴, Y. Seshimo⁵, S. Yoshioka^{6,5},

T. Iinuma¹

5 ¹Japan Agency for Marine-Earth Science and Technology, 3173-25 Showa-machi, Kanazawa-ku, Yokohama 236-0001, Japan

6 ²Graduate School of Science, Tohoku University, 6-6 Aramaki-aza-aoba, Aoba-ku, Sendai 980-8578, Japan

7 ³Independent researcher

8 ⁴Faculty of Life and Environmental Sciences, University of Tsukuba, 1-1-1 Tennodai, Tsukuba-shi, Ibaraki 305-8572, Japan

9 ⁵Department of Planetology, Graduate School of Science, Kobe University, 1-1 Rokkodai-cho, Nada-ku, Kobe, Hyogo, Japan,

10 657-8501, Japan

11 ⁶Research Center for Urban Safety and Security, Kobe University, 1-1 Rokkodai-cho, Nada-ku, Kobe 657-8501, Japan

12 **Contents of this file**

13 1. Text S1 to S2

14 2. Figures S1 to S6

15 3. Tables S1

16 **Introduction** This Supporting Information contains additional results of the numerical
17 experiments and the estimations using actual geodetic data. The posterior PDFs of the
18 underground structure estimated for SM_{smooth} in the numerical experiment are shown in

19 Figures S1. The choice of the grid spacing using an information criterion is discussed
20 in Text S1 and Table S1. The residual displacements plotted for the estimation for the
21 2010 and 2018 L-SSE are shown in Figure S2. Calculation of the slip direction based on
22 the estimation results for the rake deviation is presented in Text S2 and Figure S3. The
23 re-sampled samples for the prior PDF that from those obtained as the posterior PDF
24 estimated for the 2010 L-SSE are shown in Figure S4. The spatial distributions of the
25 number of tremor before and during the period of L-SSE are compared in Figure S5. The
26 spatial distributions of $\Delta\tau$, the shear stress change on the fault, calculated by using the
27 results of BMMFSE the smoothing model are compared in Figure S6.

28 **Text S1.**

29 In fully Bayesian inference of slip distribution without introducing regularization, a
30 significant dependence of the estimation result on the choice of the grid pattern has been
31 reported (Minson et al., 2013). Therefore, objective and quantitative determination of the
32 grid pattern, which is classified as a “model selection” problem, is desirable. Minimization
33 of minus logarithmic marginalized likelihood, or also referred to as model evidence, enables
34 an objective model selection in Bayesian inference (see Bishop (2006)). We use the widely
35 applicable Bayesian information criterion (WBIC) (Watanabe, 2013), which calculates the
36 minus logarithm marginalized likelihood approximately, obtained in the estimations for
37 the 2010 L-SSE to determine the spacing of the grid. Thus, the horizontally regular grid
38 with a spacing of 16 km is chosen as mentioned in Section 3.3. Table S1 compares WBIC
39 the various grid spacings.

40 **Text S2.**

We consider the rake deviation of the slip from the direction opposite to subduction (i.e., 125° in the north-based azimuth) as an unknown in the estimation. We obtain the random samples from the posterior PDF of the rake deviation. To compare the result with the slip direction projected to the horizontal plane estimated for the same events in Yoshioka et al. (2015), we perform a conversion from the rake deviation to slip direction. For this purpose, we need to specify the normal vector of the fault plane to define the rake angle. Because we consider a 3D plate boundary geometry, the normal vector varies depending on the location of the fault. As a representative normal vector of the main rupture area, we chose the one defined at 132.364°E and 33.026°N on the Nakanishi model (Nakanishi et al., 2018). Figure S3 shows the histograms for the slip direction in the north-based azimuth calculated based on the rake deviation from the 125° azimuth estimated for the 2010 and 2018 L-SSE based on the representative normal vector.

References

- Bishop, C. M. (2006). *Pattern recognition and machine learning*. Springer.
- Kano, M., Kato, A., & Obara, K. (2019). Episodic tremor and slip silently invades strongly locked megathrust in the Nankai Trough. *Scientific reports*, 9(1), 1–8.
- Minson, S., Simons, M., & Beck, J. (2013). Bayesian inversion for finite fault earthquake source models I—Theory and algorithm. *Geophysical Journal International*, 194(3), 1701–1726.
- Nakanishi, A., Takahashi, N., Yamamoto, Y., Takahashi, T., Citak, S. O., Nakamura, T., ... Kaneda, Y. (2018). Three-dimensional plate geometry and P-wave velocity models of the subduction zone in SW Japan: Implications for seismogenesis. *Geology and Tectonics of Subduction Zones: A Tribute to Gaku Kimura*, 534, 69.

- ⁶³ Watanabe, S. (2013). A widely applicable bayesian information criterion. *Journal of*
⁶⁴ *Machine Learning Research*, 14(Mar), 867–897.

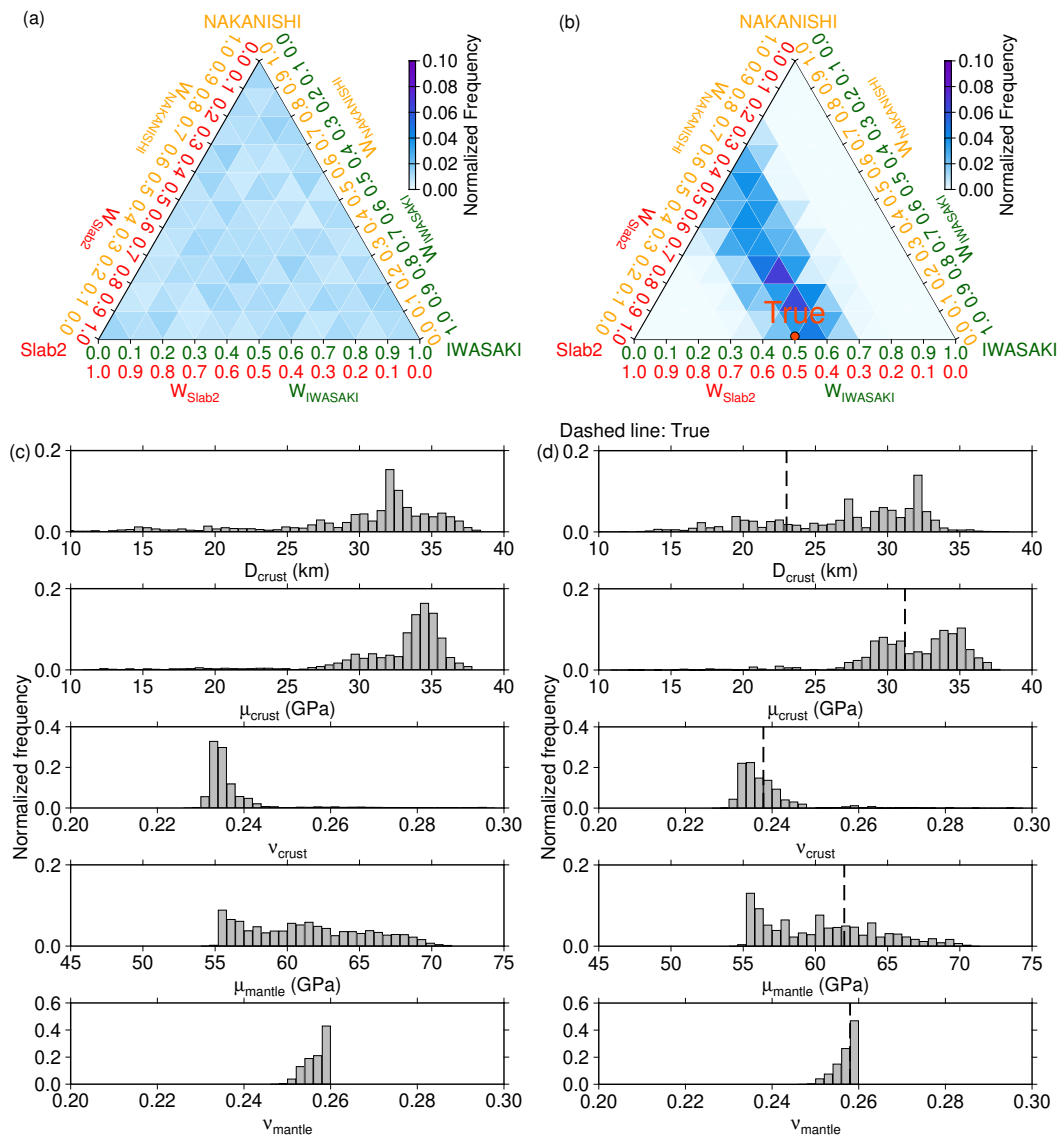


Figure S1. Comparison of the prior and posterior PDF of the underground structure in the numerical experiment for SM_{smooth} . The ternary plots for (a) the prior and (b) posterior PDF of the plate boundary geometry model. The histograms for (c) the prior and (d) posterior PDF of the elastic structure.

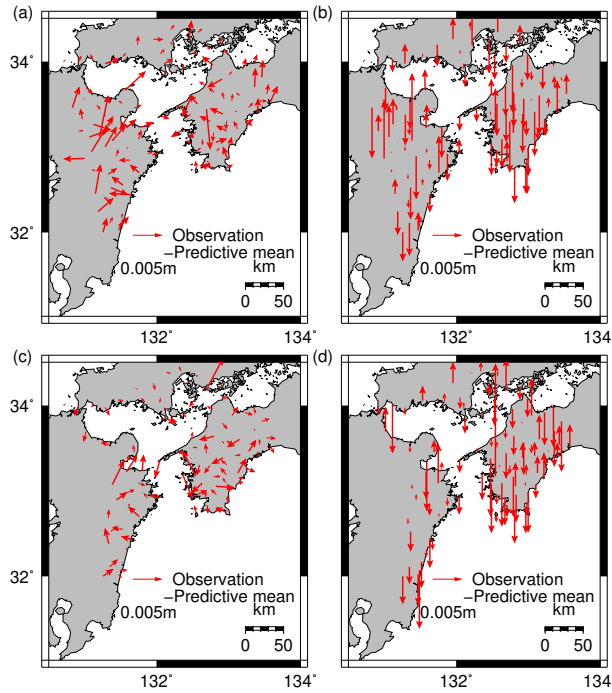


Figure S2. Residual (observation subtracted by mean of predictive mean) displacement in the estimation for the 2010 ((a) for the horizontal and (b) for the vertical component) and 2018 L-SSE ((c) for the horizontal and (d) for the vertical component).

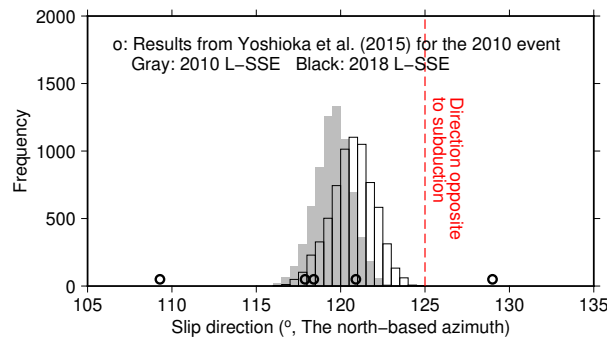


Figure S3. Histograms for the slip direction in the north-based azimuth calculated based on the rake deviation from the direction opposite to subduction (i.e., the 125° azimuth) estimated for the 2010 and 2018 L-SSE. The corresponding values in the five fault patches with the largest slip amount estimated by Yoshioka et al. (2015) for the 2010 L-SSE, denoted by black circles, are compared.

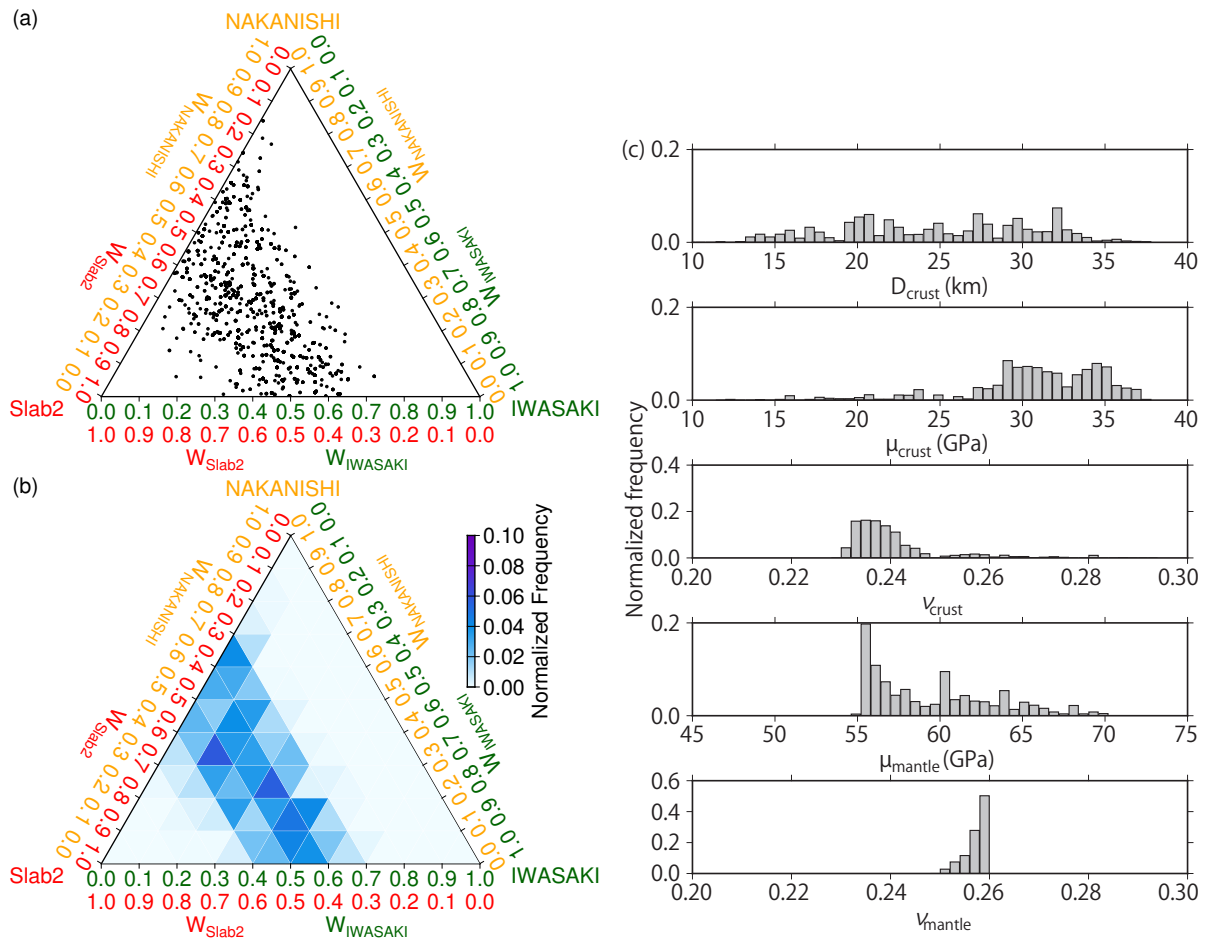


Figure S4. Samples for the prior PDF that are resampled from the samples obtained as the posterior PDF estimated for the 2010 L-SSE. (a) The plot ternary plot for the plate boundary geometry model using the dots. (b) That for the color map of normalized frequency in each small triangle. (c) The histograms for the elastic parameters.

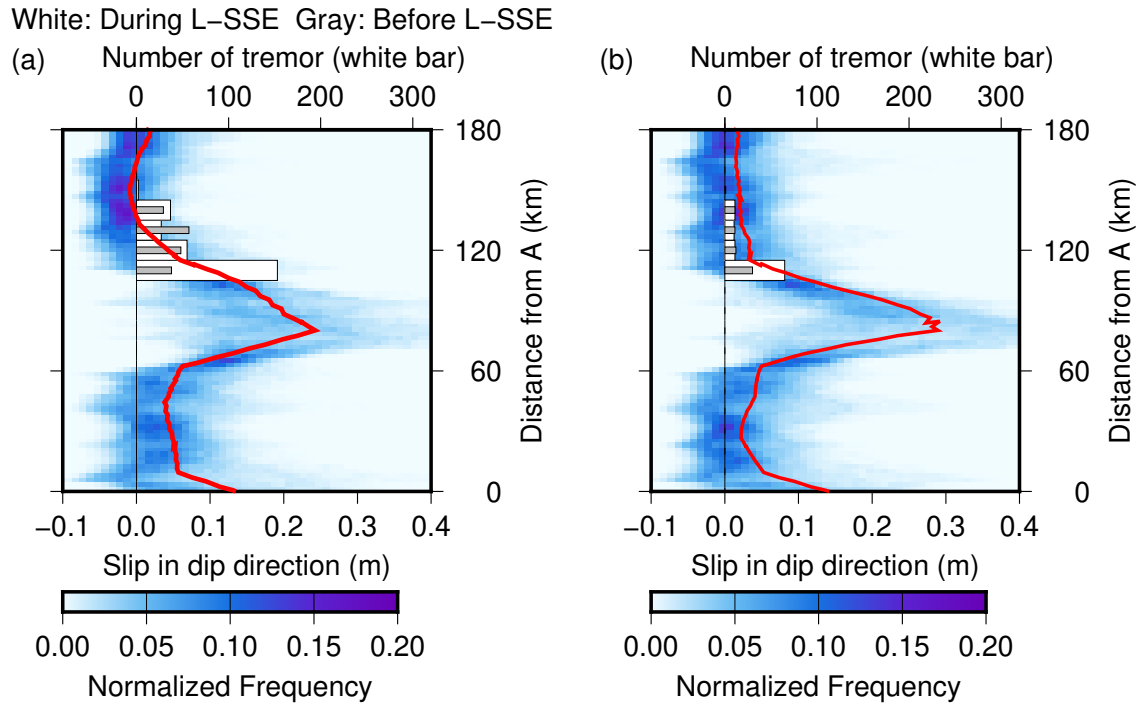


Figure S5. Comparison of the distribution of the number of tremor along the A-B line marked in Figure 10 and 11 before and during the period of L-SSE, which are denoted by the gray and white bars, respectively. (a) Those for the 2010 L-SSE. The tremors that occurred in a period between 2008.5 to 2009.5 are counted as “Before L-SSE”, and the number of tremors counted here is scaled with the duration of the 2010 L-SSE for fair comparison. We do so because the occurrence of nearby S-SSEs has been reported in September 2008 (Kano et al., 2019) and it is necessary to consider its effect on the tremor occurrence. (b) Those for the 2018 L-SSE. The tremors that occurred in a period between 2018.3 to 2018.9 are counted as “Before L-SSE”. The color map and the red line denote the frequencies of amount of slip for the posterior PDF and the mean slip distribution estimated by using BMMFSE, respectively.

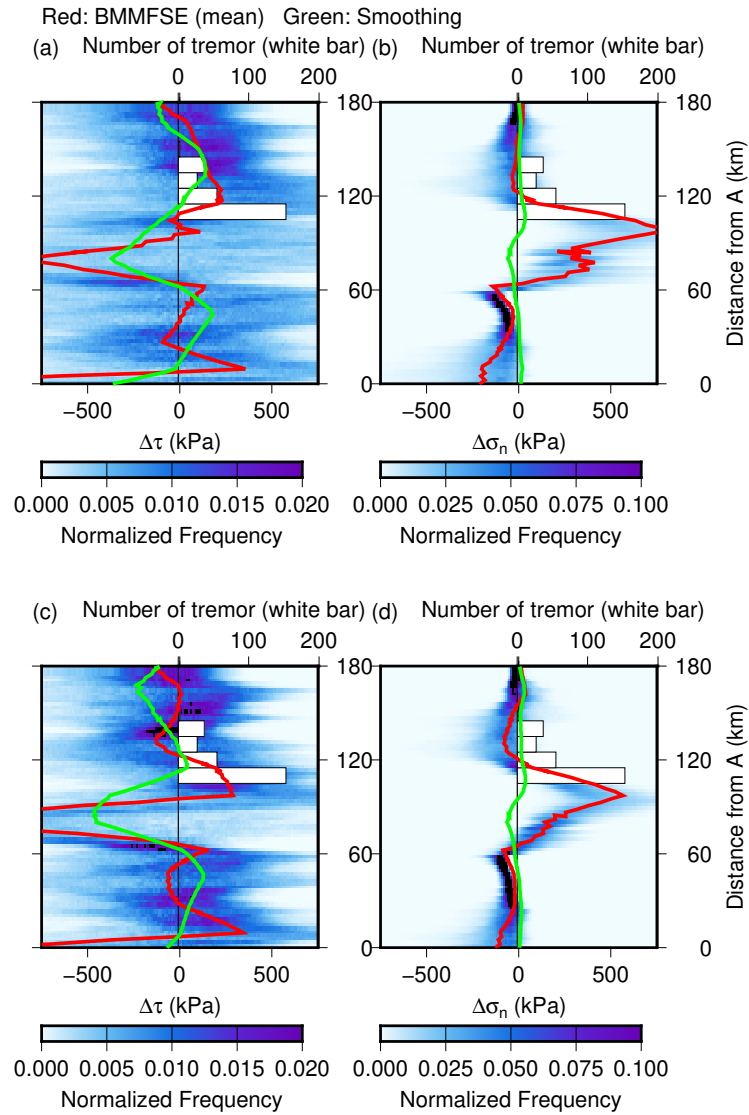


Figure S6. (a) Comparison of the distribution of $\Delta\tau$, the shear stress change on the fault, calculated using the posterior PDF for slip distribution for the 2010 L-SSE. The color map denotes the frequencies of $\Delta\tau$. The red and green line denote the distribution of $\Delta\tau$ of the mean of BMMFSE and the smoothing model, respectively. (b) Comparison of the distribution of $\Delta\sigma_n$, the normal stress change on the fault, calculated using the posterior PDF for slip distribution for the 2010 L-SSE. The color map denotes the frequencies of $\Delta\sigma_n$. The red and green line denote the distribution of $\Delta\sigma_n$ of the mean of BMMFSE and the smoothing model, respectively. In all the figures, the white bars denote the number of tremors during the L-SSE period in the area within 5 km from the line in the direction perpendicular to it. (c)(d) Those for the 2018 L-SSE.

Table S1. Comparison of WBIC calculated in the estimation for the 2010 L-SSE with different grid spacings.

Grid spacing	12 km	14 km	16 km	18 km	20 km
WBIC	-1457.79	-1458.26	-1459.02	-1458.19	-1456.95